Modeling a Small-Scale Helicopter for Simulation and Control Development

Jared Kevin Cooper

Thesis submitted to the faculty of the Virginia Polytechnic Institute and State University
in partial fulfillment of the requirements for the degree of

Master of Science
in
Mechanical Engineering

Dr. Charles F. Reinholtz, Chairman
Department of Mechanical Engineering

Dr. Alfred L. Wicks
Department of Mechanical Engineering

Dr. Craig Woolsey
Department of Aerospace and Ocean Engineering

February 22, 2006

Keywords: Rotorcraft, Unmanned Aerial Vehicles, Dynamics, Controls, Modeling, Simulation

Modeling a Small-Scale Helicopter for Simulation and Control Development

Jared Kevin Cooper

Abstract

The Virginia Polytechnic Institute and State University has recently expanded its unmanned and autonomous systems research to include aerial vehicles. In the summer of 2004, members of the Autonomous Aerial Vehicle Team at Virginia Tech successfully competed in the Student UAV competition and the International Aerial Robotics Competition. The AAVT entered a fixed-wing vehicle in the former and a rotary-wing craft in the latter competition. Commercial flight controllers were used in both competitions in order to familiarize team members with this technology. The next step in research at VT focuses on developing an experimental rotorcraft platform to be used for control algorithm testing and development.

Before the development of a flight control system is possible, a physical plant or model accurately describing the dynamics of the system is required. Use of the model in a virtual simulation environment is also beneficial to tune control gains and analyze robustness of the closed-loop system. The work presented focuses on developing a 6 degree-of-freedom model of a small-scale single shaft rotorcraft. The particular platform being developed is the Bergen Industrial Twin. In addition to dynamical concerns, attention is paid to performance characteristics of the aircraft. The nonlinear system of equations is solved which can be utilized in a simulated environment. Linear models are extracted and their control and stability characteristics are analyzed. Finally, the methodology is explained for obtaining models through system identification techniques using the CIFER facility.

Acknowledgements

Any success or achievements in my life are dependent on the support of several people. I want to thank my wonderful wife Kerri for her continual encouragement and patience throughout my time at Virginia Tech. Despite the time I spent at competitions and other activities she has always remained upbeat. My parents taught me the value of an education, persistence, and hard work early in my life and I hope this work represents their teachings.

My decision to continue in college after my undergraduate degree was strongly influenced by Dr. Charles Reinholtz. His enthusiasm and support of many senior design projects first attracted me to the unmanned discipline, and he has been a source of encouragement and mentoring ever since. I would also like to thank the 2004-05 Aerial Autonomous Team at Virginia Tech for their hard work in helping to develop Virginia Tech's first autonomous aircrafts, rotary and fixed-wing. Additionally, I would like to thank Rodney Brown for all his time and effort in test piloting multiple aircraft, some of which may have increased his blood pressure to dangerous levels. Also, I would like to thank Bruce Kothmann for sharing his technical support and knowledge of rotorcraft and answering many questions!

Table of Contents

List of Figures

List of Tables

List of Symbols

ECEF:	Earth-centered, Earth-fixed coordinate system
LTP:	Local Tangent Plane coordinate system
(Φ,Θ,Ψ):	Euler Angles (roll, pitch, yaw)
$(\lambda, \phi, h)_e$:	ECEF geodeticcoordinates (latitude, longitude, elevation)
$(x_o, y_o, z_o)_e$:	Origin in the Local Tangent Plane
$(x, y, z)_e$:	ECEF rectangluar coordinates
$(x, y, z)_{LTP}$:	Rectangular coordinates in the LTP
(x, y, z):	Vehicle body coordinate system
ϖ_{ie}:	Earth's angular rate (7.292115×10^{-5} rad/sec)
$\mathbf{R}_{eci2e}$:	Rotation from Earth Centered Inertial to ECEF
$\mathbf{R}_{e2LTP}$:	Rotation from ECEF to LTP
$\mathbf{R}_{LTP2BF}$:	Rotation from LTP to vehicle body frame
(p, q, r):	Vehicle angular rates, (roll, pitch, yaw) rad/sec
(u, v, w):	Vehicle translational velocities, m/sec
(R, M, N):	External moments (Roll, Pitch, Yaw), N-m
(X, Y, Z):	External forces acting on the vehicle CG (i, j, k), N
DOF:	Degree-of-freedom
m:	Vehicle mass, kg
$\mathbf{I_b}$:	Moment of Inertia Tensor, kg-m^2
w:	Angular rate vector, rad/sec
V:	Translational velocity vector, m/sec
l:	longitudinal distance from vehicle CG component location
h:	vertical distance from vehicle CG to component location
TPP:	Tip-Path Plane
HP:	Hub Plane
nfp:	No-feathering plane, or control plane
β:	Blade flap angle, rad/degrees
β_{1c}:	longitudinal flap angle, rad
β_{1s}:	lateral flap angle, rad
θ:	Blade pitch, rad/degrees
θ_{1c}:	Longitudinal cyclic angle
θ_{1s}:	Lateral cyclic angle
ψ_M:	Main rotor azimuth angle, rad/degree
K_β:	Torsion Spring constant, N/rad
$\lambda^2_{b:}$	Flapping frequency ratio
Ω:	Rotor speed, rad/sec
γ:	Lock Number
ρ:	Density, kg/m^3
b:	Number of blades
c:	Blade chord, m
a:	Lift curve slope, 1/rad
σ:	Rotor solidity
S_β:	Stiffness number
T:	Thrust, N

A_d: Area of rotor disc
v_1: Induced Velocity, m/sec
V_c: Climb or descent velocity, m/sec
v_{1c}: Induced velocity in vertical climb, m/sec
c_l: 2-D airfoil lift coefficient
c_d: 2-D airfoil drag coefficient
ϕ: Inflow angle, rad/degree
α: Angle of attack, rad/degree
Q: Torque, Nm
R_B: Blade radius, m
R_{Bo}: Blade offset, m
P_i: Induced Power, hp
P_p: Parasite power, hp
P_{PR}: Profile power, hp
S_β: Stiffness number, ratio of rotor stiffness to aerodynamic moment
μ: Advance ratio
f: Equivalent flat plate area, m^2
Ct: Thrust coefficient
Cq: Torque Coefficient
Cp: Power Coefficient
C_{po}: Profile Power loss
C_{pi}: Induced Power loss
τ: Time constant, sec
V_e: Total vehicle velocity relative to earth frame, m/sec
α_{sse}: Angle of attack relative to earth frame, rad
β_{sse}: Angle of sideslip relative to earth frame, rad
L: Lift, N
λ_i: Normalized inflow velocity, $v_1/\Omega R$

Subcripts:
M: Main Rotor
T: Tail Rotor
H: Horizontal Stabilizer
F: Fuselage
S: Stabilizer Rotor
B: Main Rotor Blade

Chapter 1 Introduction

This document presents the methodology used to create a model of a small-scale helicopter suitable for the development of control and obstacle avoidance algorithms, as well as animation in a simulated environment, and hardware-in-the-loop testing. A theoretical six degree-of-freedom model is developed based on first principles, and a procedure for obtaining analytical models from system identification techniques is outlined. Future research can also use the experimental model to compare/contrast first principle models and investigate ways to improve the latter.

The analytical model is based on a combined first principles and system identification technique. This hybrid technique offers a number of advantages over a traditional first principle's model. For example, in developing a rotorcraft model from physical principles, many variables are unknown or an accurate determination of their value is difficult without flight testing. Parameter estimation from input-output pairs of flight data provides these values. Furthermore, many physical models make simplifying assumptions which degrade the model's fidelity. A thorough physical model with minimal assumptions requires extensive knowledge of rotorcraft and fluid dynamics. This not only leads to an extended time of research, but also compounds the processing power required by a computer to utilize the model in any applied field such as flight control. A systems identification model makes no assumptions about the system and provides a basis to verify theoretical values with those obtained experimentally. The aircraft here considered is the Bergen Industrial Twin, single shaft helicopter.

1.1 Motivation

Over the last few decades, small-scale unmanned aerial vehicles (UAV) have increased in popularity as their unique capabilities have become better recognized. In particular, small-scale helicopters offer a desirable platform in many situations due to their vertical take off and landing ability, hover or translational flight, as well as their agility and maneuverability. Such characteristics make the scale helicopter suitable for a number of applications over a broad range of environments. Possible applications include crop surveillance and inspection, oil pipeline monitoring, security surveillance, military

reconnaissance, power line and traffic monitoring to name a few. Oftentimes, it is desirable for the UAV to be controlled autonomously, without human intervention. This situation arises when a pilot is not present or the UAV is to fly beyond the pilot's line of sight or into hostile environments. An autonomous UAV requires computer control, which in most cases, requires some dynamic model of the vehicle.

1.2 Thesis Organization

The remainder of this chapter summarizes the specifications of the Bergen Industrial Twin helicopter and the necessary modifications for measuring flight data. The goals and assumptions of the theoretical six DOF model are then outlined. Chapter 2 highlights some of the major developments in rotorcraft development, ending with the creation of Sikorsky's design of what has become known as the modern helicopter. Transformation matrices required to map body coordinate values to a local tangent plane are detailed in Chapter 3.

A majority of the rotorcraft theoretical development is found in Chapter 4, including the rigid body equations of motion and blade flapping motion. Evaluating the external force and moment contributions to the rigid body equations of motion then becomes the primary task in model development. The forces and moments generated by the main and tail rotors are provided in detail, while the contributions of the fuselage, horizontal fin, and tail fin can be found in detail in [1], [2], and [5]. Chapter 5 analyzes the hover and forward flight trim conditions of the instrumented Bergen platform. Stability analysis in hover is then treated and the associated modes of motion are identified. Finally, Chapter 6 outlines the Comprehensive Identification from FrEquency Responses (CIFER) test procedure and analysis methodology. Conclusions and future work are provided in Chapter 7.

1.3 Description of Rotorcraft Test Platform

A Bergen Industrial Twin helicopter is the platform under consideration. Table 1 summarizes the characteristics of the baseline Bergen. The salient features of the Bergen for UAV applications include its large payload capacity to weight ratio and reliability.

Table 1.1: Baseline Bergen Industrial Twin Characteristics

Length	59 inches
Height	22 inches
Dry Weight	18 pounds
Payload Capacity	25 pounds
Main Rotor Diameter	70 inches
Tail Rotor Diameter	11.8 inches
Engine	2 stroke gas Twin Cylinder 52 cc
Engine Power	8 hp
Engine RPM (hover)	10, 500
Blade RPM (hover)	1,500
Fuel Capacity	0.25 gal.
Endurance (hover)	15 minutes

The Industrial Twin utilizes a rigid rotor head and stabilizing rotor. The stabilizing rotor is a thin rod with aerodynamic paddles at the end. Most scale helicopters use this arrangement because, compared to full size helicopters, they exhibit an increased thrust and control forces to mass and moment of inertia ratios. This decreases rotor damping while increasing agility. Rotor damping arises from the rotor disc lagging the shaft in pitch and rolling motions. This produces a moment about the helicopter's center of gravity opposite and proportional to the rolling and pitching rates. A smaller time constant results in less lag, and consequently decreased damping. Thus, the small scale helicopter has an increased dynamic sensitivity to control inputs. From a control point of view, the stabilizing rotor acts like an additional input to the pilot's cyclic commands and increases damping in the rotor system. It has been shown that a majority of the rotor actuation comes as an input from the stabilizing rotor [21].

Figure 1.1: Modified Bergen in flight

Several modifications were required in order for the Bergen to be modeled analytically. Primarily, instrumentation was added capable of measuring the vehicle's response to test inputs. Because of the size of the avionics package, custom landing gear was fabricated. A tailored electronics package was also developed that provides redundant power and battery monitoring to the necessary components. Figure 1.1 illustrates the Bergen with modifications.

1.3.1 Instrumented Platform

The Bergen platform was originally purchased to serve as a platform in the 2005 International Aerial Robotics Competition, sponsored by the Autonomous Unmanned Vehicle System, International (AUVSI) (www.auvsi.com). A majority of the modifications to the Bergen were performed by the 2004-05 Autonomous Aerial Vehicle Team (AAVT) at Virginia Tech. A detailed description of the system's development is beyond the scope of this work but can be found in [13].

The various sensors and power circuitry added a total avionics weight of 14 pounds, including fuel.. Thus, the platform has a gross take-off weight of 32 pounds. Accurate values of the center of gravity and moments of inertia are critical to the model's fidelity. The center of gravity was determined experimentally by using 2 scales [15]. The moment of inertia tensor was found by using a Trifilar Pendulum for the yaw and pitch axes, and a Bifilar Pendulum for the roll axis. These values are reported in Table 1.2. The I_{xy} and I_{zy} cross moments of inertia are zero by symmetry and I_{xz} is assumed negligible. A detailed description of the test methods can be found in Appendix A [14, 15].

Table 1.2: Center of Gravity and Inertial Parameters

Parameter	Value
xcg	22.5 inches
ycg	0 inches
zcg	13.4 inches
Ixx	0.32 kg*m^2
Iyy	1.43 kg*m^2
Izz	1.21 kg*m^2

1.4 Model Goals and Assumptions

In general, the accuracy of any mathematical model depends on the end use. In a complex system such as a helicopter a number of interacting subsystems complicate the ability to accurately describe the dynamics theoretically. For example, the main rotor is the primary generator of aerodynamic forces in any flight condition and controls the main forces and moments dictating aircraft position, velocity, and attitude. Due to this fact, an extensive amount of ongoing research aims to describe the rotor-fuselage coupling and the effect downwash has on this interaction. Other research predicts with evermore complexity the blade flap motion and explains how blade flap creates a non-uniform downwash as the blade rotates [2]. Quickly, the growing complexity of a program which seeks to accurately describe the main rotor alone becomes apparent. Additionally, models describing the fuselage, empennage, and tail rotor can also exponentially increase the overall model's complexity.

In addition to the complex programming necessary to create a model of this fidelity, a high degree of aerodynamic understanding is required. Some areas in rotorcraft operation are not yet well described by theory. One example is cross-coupling effects of the main rotor. In [5] the cross-coupling effects from the simulation model were removed to better match flight data. At some point the costs of continually adding detail to the model outweighs the benefits.

For simulation and control purposes an accurate model can be developed using a six degree-of-freedom representation. This modeling technique employs a quasi-static assumption for the main rotor which eliminates three states corresponding to blade motion as separate degrees of freedom. This assumption is validated because the main rotor's time constant is much faster than the rigid body dynamics. The simulated rotor then changes forces and moments simultaneously in response to flight conditions and control inputs. However, only low bandwidth flight control can be achieved with this model. Tischler has verified that for high bandwidth control, a hybrid nine DOF is required. In the hybrid model blade coning, lateral and longitudinal flapping are modeled as separate states. Further details can be found in [8]. Most remote control helicopters also use a yaw control gyro which adds another degree of freedom plus a stabilizing rotor

(modeled as a teetering rotor) adding two degrees of freedom, all resulting in a model with 11 degrees of freedom.

This work endeavors to create a six DOF theoretical model. The methodology for using the Comprehensive Identification from FrEquency Responses (CIFER) facility to extract analytical 11 DOF models is also provided. These will cover hover and forward flight. The features of the six DOF theoretical model are:

- First order main rotor flapping dynamics (uncoupled from body)
- Root cut-out effects ignored
- Tip losses are included
- Thrust vector is perpendicular to the tip path plane
- Reverse flow region is neglected (only seen in forward flight)
- Uniform rotor downwash
- Realistic power consumption including the tail rotor.

In developing this model, the nonlinear equations of motion are solved which can be used for real-time simulations. This set of equations is then linearized around the hover trim condition. The resulting linear model can be used in developing linear control techniques and analyzing stability.

Chapter 2 History of Rotorcraft Development

This chapter summarizes some of the salient developments in rotorcraft history. The work here only highlights some of the major developments. Further reading can be found in [4] and [10].

2.1 Rotorcraft History

A great amount of literature on rotary wing development exists. Many historians attribute the first idea of vertical flight to the Chinese (400 BC), evidenced by what are now called Chinese tops. The concept of a vertically flying machine capable of transporting man is accredited to Leonardo da Vinci based on his "air screw" device dated to 1483. Figure 2.1 illustrates da Vinci's device which has strong similarities to Archimedes' water screw [10].

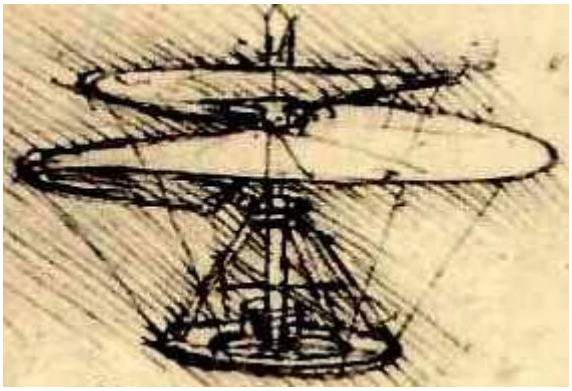

Figure 2.1: Leonardo da Vinci's Airscrew

Development continued throughout the centuries but was hindered by a number of challenges. Primary challenges included a lack of understanding the complex aerodynamic nature of rotary-wing flight, the inability to develop a power plant exhibiting a high power density, and inherent aerodynamic vibration. By the late 1800s, some of these problems were better understood, and in 1878 an Italian professor of civil engineering, Enrico Forlanini, constructed a steam-driven model weighing 7.7 pounds. In 1907, four years after the Wright brothers' first successful fixed-wing flight, Paul Cornu of France constructed the first vertical flying machine to lift a human from the earth. The Cornu helicopter is shown in Figure 2.2 [10]. The machine consisted of two rotors and small wings beneath the rotors to provide simple flight control.

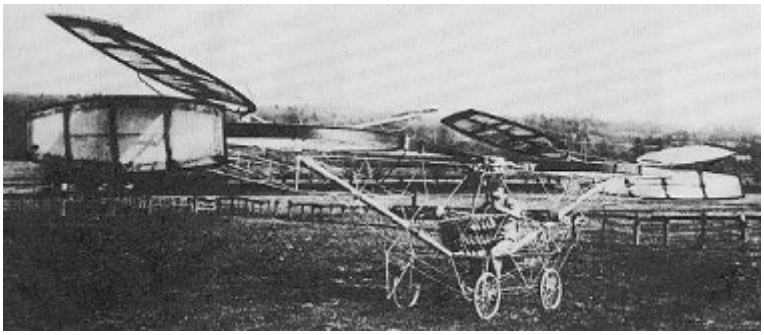

Figure 2.2: Cornu Helicopter (www.aerospaceweb.org)

Around that same time, in 1909, Emile and Henry Berliner constructed a coaxial helicopter in the United States, shown in Figure 2.3. Despite these achievements, controlling the helicopter was still difficult and the available power plants lacked sufficient power to weight ratio for sustained flight.

Figure 2.3: Berliner Coaxial Helicopter (www.centennialofflight.gov)

In 1937, a German engineer, Dr. Heinrich Focke built the most successful vertical flying machine to date. He used two rotors side by side rotating in opposite directions and inclined inward to provide dihedral stability much like wings of a fixed-wing craft. Figure 2.4 depicts Focke's machine. He also incorporated a swash plate, cyclic control mechanism to achieve longitudinal stability. Yaw control and stability were achieved by a vertical rudder and horizontal tail. This was the first helicopter that showed sustained and useful flight. The Focke helicopter set records for flight duration (80 minutes), altitude (11,200 feet), speeds (75 miles per hour) and distance (143 miles). Up to this point, many of these records were held by a similar machine undergoing parallel

development, called the autogiro. Juan de la Cierva of Spain pioneered this development and created a machine which accounted for many rotary wing principles such as blade flap and hinged-rotors. These topics will be discussed in greater detail later as they apply to the current work.

Figure 2.4: Focke's dual rotor helicopter (www.eurocopter.com)

The birth of the modern helicopter occurred in 1941 when Igor Sikorsky produced the VS-300 helicopter which surpassed all records held by Focke. The initial Sikorsky design employed one main rotor and three auxiliary rotors, one vertical and two horizontal at the tail. After many design iterations, the VS-300 emerged as the single main-tail rotor configuration popular in many helicopters today. The tail rotor acts as a counter torque device and provides yaw control and stability [4]. Because most scale helicopters employ this design, it will be the focus of model development.

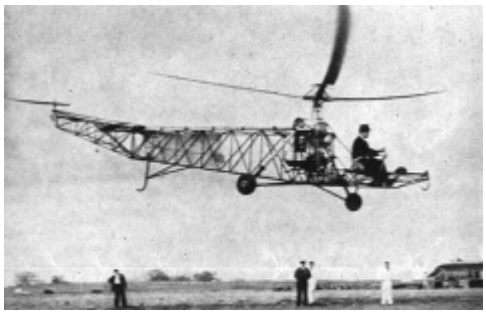

Figure 2.5 (a) Sikorsky pilots a conceptual design

Figure 2.5 (b) First helicopter used in combat Sikorsky R-4 (www.centennialofflight.gov)

Chapter 3 Coordinate Frames and Transformation

A number of coordinate frames are available for simulation purposes. The primary coordinate frames of interest as applied to this thesis are now summarized. The transformation between various coordinate frames is derived with a focus on mapping from the body coordinate system to the local tangent plane and vice versa. This is of particular interest because it relates vehicle velocities, accelerations, and attitude to an assumed flat and stationary earth position used in simulation modeling.

3.1 Coordinate Frame Definition

The problem of relating an aerial vehicle to a fixed reference point involves a number of coordinate transforms. Different coordinate systems are desirable as each offers advantages for specific calculations. For example, a fixed coordinate system is advantageous for tracking motion and velocity of a vehicle. On the other hand, in deriving equations of motion, one requires an inertial frame where Newton's Laws hold. Sensors, including accelerometers and gyroscopes, report data in an inertial coordinate system. Yet these sensors are normally located on the vehicle; therefore, a body coordinate system is also defined, located at the vehicle's center of mass. Still, other sensors, such as a Global Positioning System (GPS) often report in a different frame. Figure 3.1 summarizes the challenge.

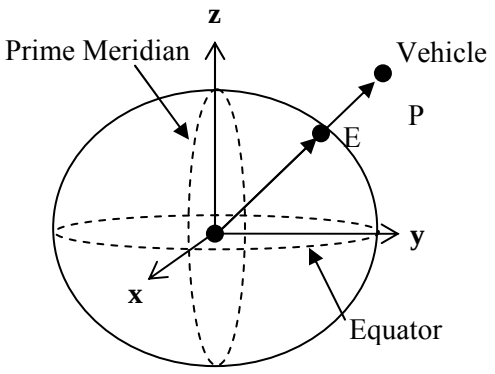

Figure 3.1: Earth Model

The vehicle's position is at an arbitrary point P above the Earth's surface. Point E defines the position of P relative to the Earth's surface. Such a coordinate system is known as the Earth-centered earth-fixed (ECEF) frame. As the name implies, the center of this coordinate frame is fixed to the center of the earth; therefore the axes rotate relative to the inertial frame with the same frequency as the earth, $\varpi_{ie} = 7.292115 \times 10^{-5}$ rad/sec.

The rotation from an Earth Centered Inertial (ECI) frame to the ECEF is just a rotation about the z axis

$$R_{eci2e} = \begin{bmatrix} \cos\varpi_{ie}t & \sin\varpi_{ie}t & 0 \\ -\sin\varpi_{ie}t & \cos\varpi_{ie}t & 0 \\ 0 & 0 & 1 \end{bmatrix} \tag{3.1}$$

where t is the time since the beginning of simulation or navigation. In defining such a system, efforts have been made to approximate the Earth's geoid. Typically, an ellipsoid is used rotated about its minor axis. A detailed derivation can be found in [7]. Position can be expressed in rectangular or geodetic coordinates in the ECEF system. Rectangular coordinates $(x, y, z)_e$ have the the x axis extended through the intersection of the prime meridian and equator, the z-axis cuts through the true north pole, and the y-axis completes the right hand coordinate system, passing through the equator.

The ECEF geodetic coordinates are based on the approximated geoid which has been measured at different times. One measurement known as the World Geodetic System was conducted in 1984 (WGS-84) and is used in many GPS systems today. Geodetic coordinates express position as $(\lambda, \phi, h)_e$ where λ_e represents latitude, ϕ_e longitude, and h_e altitude. Transformations between the two systems exist and can be found in [7].

Another convenient reference frame is known as the local geodetic or tangent plane. This frame refers to the "north, east, down" directions we commonly use in everday life. A tangent plane is attached to the ECEF geodetic ellipsoid at the desired point, convinient for local measurements. The attached point becomes the origin of the local frame. The x-axis points toward true north, the y-axis east, and the z-axis completes the right had coordinate frame pointing toward the interior of the earth, perpendicular to the ellipsoid. Figure 3.2 illustrates the local tangent plane.

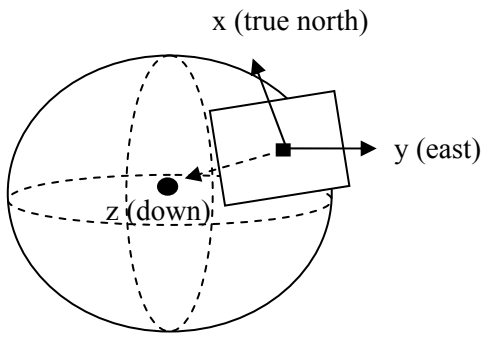

Figure 3.2: Local tangent plane coordinate

The local tangent plane is useful for local navigation, moreso than ECEF coordinates. However, sensor information is oftimes reported in ECEF coordinates and a transformation to the local tangent plane is necessary.

3.2 Coordinate Frame Transformation

The transformation from ECEF to local tangent plane coordinates is accomplished by first choosing an origin in the local tangent plane $(x_o, y_o, z_o)_e$, i.e., point E in Figure 3.1. Then $(x, y, z)_e$ is point P in Figure 3.1 whose coordinates are known through GPS measurement. Point P's coordinates in the local tangent plane (LTP) are found by

$$\begin{Bmatrix} x \\ y \\ z \end{Bmatrix}_{LTP} = \begin{bmatrix} -\sin(\lambda)\cos(\phi) & -\sin(\lambda)\sin(\phi) & \cos(\lambda) \\ -\sin(\phi) & \cos(\phi) & 0 \\ -\cos(\lambda)\cos(\phi) & -\cos(\lambda)\sin(\phi) & -\sin(\lambda) \end{bmatrix} \left(\begin{bmatrix} x \\ y \\ z \end{bmatrix}_e - \begin{bmatrix} x_o \\ y_o \\ z_o \end{bmatrix}_e \right)$$
$$\begin{Bmatrix} x \\ y \\ z \end{Bmatrix}_{LTP} = \mathbf{R}_{e2LTP} \left(\begin{bmatrix} x \\ y \\ z \end{bmatrix}_e - \begin{bmatrix} x_o \\ y_o \\ z_o \end{bmatrix}_e \right) \tag{3.2}$$

Transforming from the LTP to ECEF is accomplished by taking the inverse of $\mathbf{R}_{e2LTP}$ which is simply the transpose.

To this point relationships between a global and local frame suitable for local navigation and simulation have been established. The vehicle body frame is another important coordinate system. The body system is defined with the origin at the center of mass of

the vehicle, and the x, y, and z axis pointing forward toward the helicopter's nose, starboard, and downwards, respectively. The body frame is used in developing equations of motion. Inertial sensor output must be transformed to the LTP. Traditionally in flight dynamics this transformation is accomplished by three successive rotations of the Euler angles about the yaw, Ψ, pitch, Θ, and roll, Φ axes as shown in Figure 3.3.

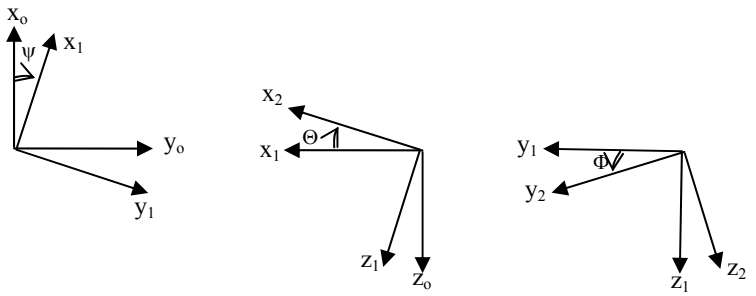

Figure 3.3: Successive rotations form the rotation matrix

The transformation matrix, $\mathbf{R}_{LTP2BF}$, relating the LTP to body frame coordinates is then

$$R_{LTP2BF} = \begin{bmatrix} \cos\Theta\cos\Psi & \cos\Theta\sin\Psi & -\sin\Theta \\ \sin\Phi\sin\Theta\cos\Psi - \cos\Phi\sin\Psi & \sin\Phi\sin\Theta\sin\Psi + \cos\Phi\cos\Psi & \sin\Phi\cos\Theta \\ \cos\Phi\sin\Theta\cos\Psi + \sin\Phi\sin\Psi & \cos\Phi\sin\Theta\sin\Psi - \sin\Phi\cos\Psi & \cos\Phi\cos\Theta \end{bmatrix} \tag{3.3}$$

Two very useful applications of $\mathbf{R}_{LTP2BF}$ in simulation and control come from relating the body velocities and accelerations to a fixed reference earth point. For example, the time rate of change of the Euler angles and the fuselage angular rates (p, q, r). A similar process used to find $\mathbf{R}_{LTP2BF}$ is employed and results in [2]

$$\begin{Bmatrix} \dot{\Phi} \\ \dot{\Theta} \\ \dot{\Psi} \end{Bmatrix} = \begin{bmatrix} 1 & \sin\Phi\tan\Theta & \cos\Phi\tan\Theta \\ 0 & \cos\Phi & -\sin\Phi \\ 0 & \left(\frac{\sin\Phi}{\cos\Theta}\right) & \left(\frac{\cos\Phi}{\cos\Theta}\right) \end{bmatrix} \begin{Bmatrix} p \\ q \\ r \end{Bmatrix} \tag{3.4}$$

with the inverse given by

$$\begin{Bmatrix} p \\ q \\ r \end{Bmatrix} = \begin{bmatrix} 1 & 0 & -\sin\Theta \\ 0 & \cos\Phi & \sin\Phi\cos\Theta \\ 0 & -\sin\Phi & \cos\Phi\cos\Theta \end{bmatrix} \begin{Bmatrix} \dot{\Phi} \\ \dot{\Theta} \\ \dot{\Psi} \end{Bmatrix} \tag{3.5}$$

Equation 3.4 allows one to integrate the Euler angle derivatives and resolve the vehicle attitude in the LTP. Singularities occur at ±90°, but this does not pose a problem under normal flight conditions.

Chapter 4 Basic Rotorcraft Aerodynamics

Theoretical rotorcraft aerodynamics has been studied for some time and is generally understood. A review of the fundamental concepts, as they apply to the model under development, is given here. A more in depth discussion can be found in [1], [2], and [5].

4.1 Rotorcraft Overview

From a modeling standpoint, the helicopter can be broken into a set of subsystems. These include the main rotor, fuselage or body, empennage, and tail rotor. Each of these subsystems creates forces and/or moments that contribute to the overall vehicle dynamics. Figure 4.1 illustrates each of these subsystems and the forces or moments they produce. The empennage is composed of a horizontal and vertical stabilizer. Combinations of aerodynamic, inertial and gravitational forces are responsible for the helicopter's dynamics.

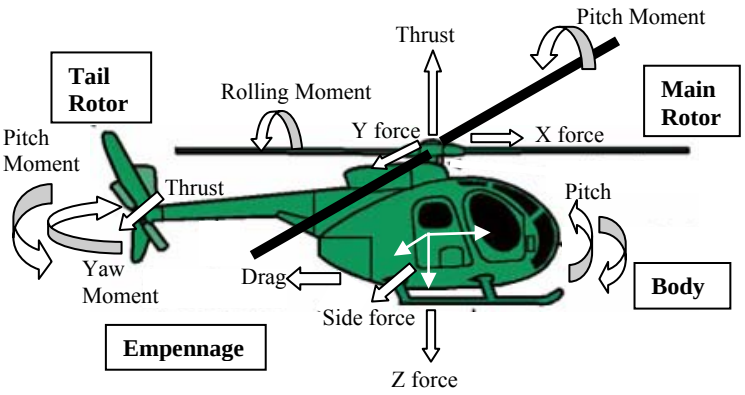

Figure 4.1: Subsystem of components comprising the helicopter with respective moments and forces (www.centennialofflight.gov)

It should be noted that conventional full scale helicopters have a counterclockwise rotating main rotor when viewed from above. Scale helicopters normally employ a clockwise rotation. This difference can be accounted for with a change of sign in the dynamic equations where appropriate. For example, the torque developed by the main rotor is in the opposite direction, and therefore, the anti-torque developed by the tail rotor is also in the opposite direction. Derivations can therefore be carried out by traditional techniques with suitable modifications. A qualitative overview of the contribution of each subsystem is provided in Table 4.1 [5].

Table 4.1: Summary of component contribution

Component	Physical Contribution	Response Characteristic
Main Rotor	Thrust	1st order flapping (decoupled)
	Torque	Power Required
	Induced Velocity	Trim
	Induced Power	Phugoid
	Profile Power	Dihedral
	No off-axis flapping stiffness	Pitch Mode Roll Mode
	Constant RPM	Min. Cross-Coupling
Tail Rotor	Thurst	Trim
	Torque	Power Required
	Induced Velocity	Roll Mode
	Induced Power	
	Profile Power	
Fuselage	Center of Gravity	Trim
	Moments of Inertia	Power Required
	Parasite Power	Min. Cross-Coupling
	Cross Moments neglected	
Horizontal Fin	Lift	Short Period
	Vertical Drag	Trim
		Pitch Mode
		Power Required
Vertical Fin	Lift	Dutch Roll
		Roll Mode

Before detailing how these forces and moment are generated, it is worthwhile to explain the coordinate system used in the analysis. For deriving equations of motion it is convenient to use body axes, since the inertias remain constant. The traditional vehicle axes and associated forces and moments are displayed in Figure 4.2.

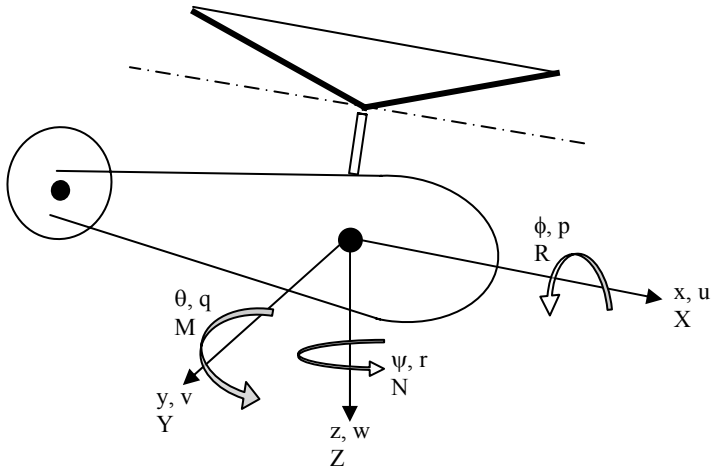

Figure 4.2: Body coordinate system with associated forces and moments

In Figure 4.2, the three translational velocities, (u, v, w) are shown as well as the three angular rates (p, q, r), and the Euler angles (Φ, Θ, Ψ). The velocities are referenced to the vehicle CG and can be related to the LTP using the described methods, while the Euler angles are referenced to an earth fixed reference system.

4.2 Main Rotor Reference Planes

The main rotor is the principal component in the helicopter system and is the primary factor in the analysis of power, stability, and control. In rotor dynamics analysis, three reference planes have been commonly used: the hub, or shaft, plane, the tip-path plane (TPP), and the no-feathering, or control, plane. The hub plane has the x and y axis parallel to the body frame, with the z axis pointing downwards with the rotor shaft. The tip-path plane is formed by the blade tips as shown in Figure 4.3. β_{1c} and β_{1s} refer to the longitudinal and lateral tilt of the TPP respectively. θ_{1c} and θ_{1s} refer to the lateral and longitudinal cyclic pitch commanded by the pilot. One simplifying assumption is that the thrust vector is always perpendicular to the TPP. This is true in hover and vertical flight and accurate in forward flight [2].

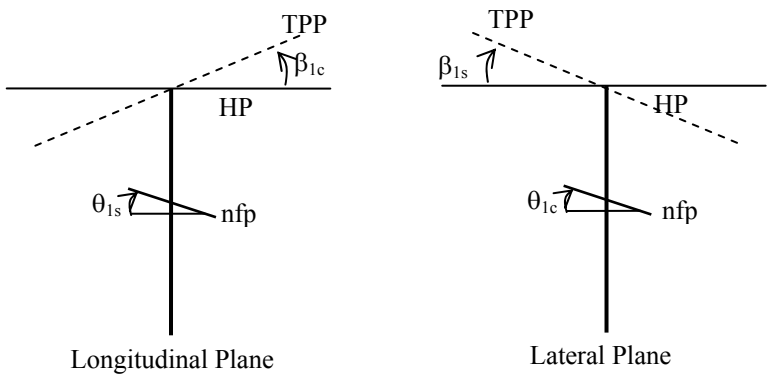

Figure 4.3: Main rotor reference frames

It is often convenient to express the forces and moments generated by the rotor in the TPP and then transform them to the hub plane or directly to the body axes. Once transformed, the forces and moments are added to the components acting on the rigid body.

4.3 Rigid Body Equations of Motion

The helicopter obeys Newton's Laws of Motion just as any other rigid body. The rigid body equations of motion are developed assuming a flat, stationary earth reference plane. Considering the low altitude of the helicopter and short flight times, this is a reasonable assumption. The earth reference plane can then be used as an inertial frame. The rigid body equations of motion and kinematic equations are expressed in the body frame as

$$\mathbf{F} = m\left(\dot{\mathbf{V}}_{bf} + \mathbf{w}_{bf} \times \mathbf{V}_{bf}\right) \tag{4.1}$$

$$\mathbf{M} = \mathbf{I}_b \dot{\mathbf{w}}_{bf} + \mathbf{w}_{bf} \times \mathbf{I}_b \mathbf{w}_{bf} \tag{4.2}$$

where $\mathbf{I_b}$ is the moment of inertia tensor. A derivation can be found in [2] and [3]. Due to symmetry, the cross moments I_{xy} and I_{zy} are zero. The I_{zx} cross moment is assumed to be zero in the final analysis, but will be included here. The components of the external force vector **F** and moment vector **M** are the summed contributions of each subsystem in the given direction. Expanding the right hand side of equation yields

Force Equations

$$
\begin{aligned}
X &= m\left(g\sin\theta + \dot{u} + \left(qw - rv\right)\right) \\
Y &= m\left(-g\cos\theta\sin\phi + \dot{v} + \left(ru - pw\right)\right) \\
Z &= m\left(-g\cos\theta\cos\phi + \dot{w} + \left(pv - qu\right)\right)
\end{aligned}
\qquad \text{(4.3 a-c)}
$$

Moment Equations

$$
\begin{aligned}
R &= I_{xx}\dot{p} - I_{zx}\dot{r} + \left(I_{zz} - I_{yy}\right)qr - I_{zx}pq \\
M &= I_{yy}\dot{q} + \left(I_{xx} - I_{zz}\right)rp + I_{zx}\left(p^2 - r^2\right) \\
N &= I_{zz}\dot{r} - I_{zx}\dot{p} + \left(I_{yy} - I_{xx}\right)pq + I_{zx}qr
\end{aligned}
\qquad \text{(4.3 d-f)}
$$

Each component of **F** has contributions from the main rotor, tail rotor, horizontal stabilizer, vertical stabilizer, fuselage, and wing, if applicable. Denoting these explicitly expands the force and moment equations to

$$
\begin{aligned}
&X_M + X_T + X_H + X_V + X_F = m\left(g\sin\theta + \dot{u} + \left(qw - rv\right)\right) \\
&Y_M + Y_T \qquad\quad + Y_V + Y_F = m\left(-g\cos\theta\sin\phi + \dot{v} + \left(ru - pw\right)\right) \\
&Z_M + Z_T + Z_H + Z_V + Z_F = m\left(-g\cos\theta\cos\phi + \dot{w} + \left(pv - qu\right)\right) \\
&R_M + Y_M h_M + Z_M y_M + Y_T h_T + Y_V h_V + Y_F h_F + R_F = I_{xx}\dot{p} - I_{zx}\dot{r} + \left(I_{zz} - I_{yy}\right)qr - I_{zx}pq \\
&M_M - X_M h_M + Z_M l_M + M_T - X_T h_T + Z_T l_T - X_H h_H + Z_H l_H - X_V h_V + M_F + Z_F l_F - X_F h_F = \\
&\qquad I_{yy}\dot{q} + \left(I_{xx} - I_{zz}\right)rp + I_{zx}\left(p^2 - r^2\right) \\
&N_M - Y_M l_M - Y_T l_T - Y_V l_V + N_F - Y_F l_F = I_{zz}\dot{r} - I_{zx}\dot{p} + \left(I_{yy} - I_{xx}\right)pq + I_{zx}qr
\end{aligned}
\qquad \text{(4.4 a-f)}
$$

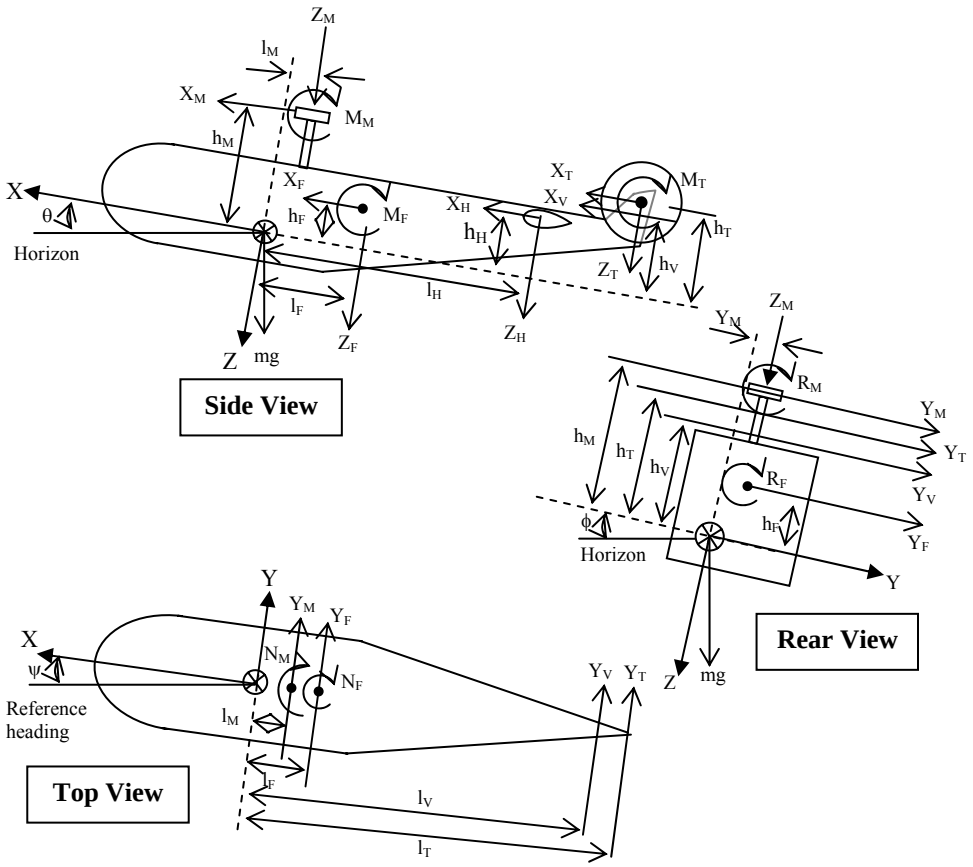

Figure 4.4: Each component contributes to the overall vehicle dynamics

Figure 4.4 illustrates the individual forces and moments from each subsystem. The modeling and simulation problem now reduces to discovering the force and moment components. It should be noted that the Bergen has a CG aft of the main rotor shaft and a fuselage aerodynamic center fore of the CG. Therefore, any contributions with an 'l_m' or 'l_f' will be negated in the above equations. For example, referencing Figure 4.4 a CG fore of the main rotor shaft has a negative pitching moment (the $Z_m l_m$ term) but a CG located aft of the shaft will cause the nose to pitch upwards.

Once the forces and moments are determined, the vehicle's velocities and accelerations can be found in the body coordinate system. Using the transformation matrices developed earlier, the complete set of kinematic equations for motions of the aircraft center of gravity referenced to a flat, non-rotating earth is [12]

$$
\begin{aligned}
\dot{u}_e &= rv - qw + a_x - g\sin\theta \\
\dot{v}_e &= pq - ru + a_y + g\cos\theta\sin\phi \\
\dot{w}_e &= qu - pv + a_z + g\cos\theta\cos\phi \\
\dot{\phi} &= p + q\sin\phi\tan\theta + r\cos\phi\tan\theta \\
\dot{\theta} &= q\cos\phi - r\sin\phi \\
\dot{\varphi} &= q\sin\phi\sec\theta + r\cos\phi\sec\theta \\
\dot{x}_e &= u\cos\theta\cos\phi + v\left(\sin\phi\sin\theta\cos\varphi - \cos\phi\sin\varphi\right) + w\left(\cos\phi\sin\theta\cos\varphi + \sin\phi\sin\varphi\right) \\
\dot{y}_e &= u\cos\phi\sin\varphi + v\left(\sin\phi\sin\theta\sin\varphi + \cos\phi\cos\varphi\right) + w\left(\cos\phi\sin\theta\sin\varphi - \sin\phi\sin\varphi\right) \\
\dot{z}_e &= -u\sin\theta + v\cos\theta\sin\phi + w\cos\theta\cos\phi \\
V_e &= \sqrt{u^2 + w^2 + v^2} \\
\alpha_{sse} &= \arctan\left(\frac{w}{u}\right) \\
\beta_{sse} &= \arctan\left(\frac{v}{u}\right)
\end{aligned}
\qquad \text{(4.5 a-l)}
$$

4.4 Rotor Head Design and Blade Motion

Three main rotor head designs are common in helicopter design: (1) articulated, (2) teetering, and (3) hingeless or rigid. The Bergen incorporates a rigid teetering rotor design and stiff restraints as illustrated in Figure 4.5. Such a design results in a helicopter with greater agility than full scale craft and influences the flapping characteristics which are now discussed.

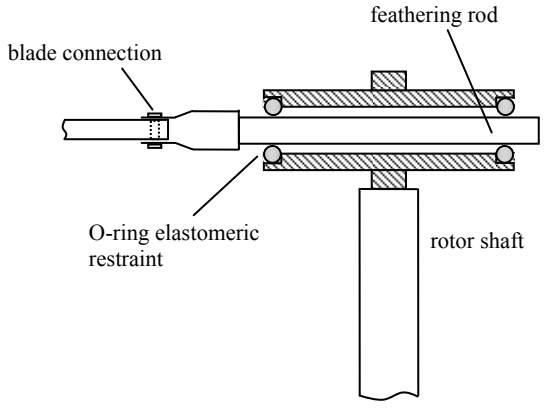

Figure 4.5: Bergen's rigid rotor design

4.4.1 Blade Motion

Blade motion can be described as a function of flap and pitch angle as depicted in Figure 4.6. There is also an in-plane lead-lag angle which is neglected. The flapping angle, β, is an important parameter in describing the motion of the main rotor blades. The blade pitch, θ, is another important variable describing the rotation of the blade about an axis in the disk plane parallel to the blade quarter chord line. Both are complex functions of aerodynamic and inertial forces.

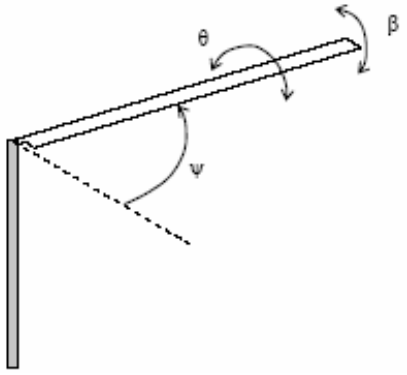

Figure 4.6: The blade motion is described by the azimuth, flap, and pitch angle

Blade flapping occurs as the rotor blades seek an equilibrium condition as they rotate about the rotor shaft. The forward flight condition provides an appropriate example of the importance of blade flap. The velocity acting along the blade is now a function of the radial position and azimuth angle, with zero azimuth position over the tail. As the advancing blade propagates it encounters a larger velocity component, due to the vehicle velocity, than the retreating side. This creates an unequal lift distribution on the advancing and retreating blades. It also causes the advancing blade to accelerate upward, until it is positioned over the nose, at which point the blade reaches maximum displacement. The retreating blade goes through a similar motion, except it translates downward until it is over the tail. The upwards movement of the advancing blade decreases its angle of attack, while the retreating blade's angle of attack is increased. In this manner, blade flapping produces an equilibrium lift distribution. Neglecting cross-coupling effects, the phase angle between aerodynamic input and maximum output is 90 degrees and the rotor is modeled as a system in resonance.

To explicitly account for β one must consider a combination of inertial, aerodynamic, and dynamic forces. Figure 4.7 shows a rotor with a restoring force $K_\beta\beta$, centrifugal force, $-\Omega^2 r$, and inertial force, $r\beta$. The flapping motion sets these moments to zero at the hinge, resulting in the mathematical model [2]

$$\begin{aligned} K_\beta \beta &= -\int_0^R rm(r)\left\{r\ddot{\beta} + r\Omega^2\beta\right\}dr \\ \ddot{\beta} &+ \beta\left(\frac{K_\beta}{I_b} + \Omega^2\right) = 0 \end{aligned} \tag{4.6}$$

where I_b is the blade flapping moment of inertia, defined as

$$I_b = \int_0^R r^2 m(r)dr = \frac{R^2}{3}M \tag{4.7}$$

m(r) is the mass per radial position, and M is the total blade mass. Equation 4.6 can be redefined by differentiating β with respect to $\psi = \Omega t$. Representing this spatial differentiation with a prime character yields

$$\begin{aligned} \beta'' + \beta\lambda_b^2 &= 0 \\ \lambda_b^2 &= \frac{K_\beta}{\Omega^2 I_b} + 1 \end{aligned} \tag{4.8}$$

where λ^2_b is the flapping frequency ratio. This is the ratio of the flapping motions natural frequency to Ω. When K_β is zero, as in a hingeless rotor, the frequency ratio is unity and the blade flap has a natural frequency equal to Ω. In this scenario, the rotor acts like a system in resonance and the phase angle is exactly 90°. There will be no tendency for the shaft to tilt in response to flapping as moments are not transmitted to the hub and fuselage. With nonzero K_β and the addition of a hinge offset (or effective hinge offset) the frequency ratio is greater than one and the phase angle is less than 90°. The natural frequency of the flapping motion is faster than Ω. In this scenario, the blades find a new equilibrium position when affected by a disturbance or input in less than one revolution.

Accounting for hinge offset results in a flapping frequency ratio of 1.28. The rotor stiffness is then found to be 176 Newton meters per radian. Using flight data charts in [1] the phase angle, ϕ, is then estimated to be 74˚. This reduction is phase angle is evidence of flap cross-coupling effects. The magnitude of the coupling can be estimated by [1]

$$\frac{\beta_{1s}}{\beta_{1c}} = -\cot\phi \tag{4.9}$$

This means that a 1˚ change in longitudinal flapping is accompanied by a lateral flapping of -0.28˚ for a counterclockwise blade rotation and 0.28˚ lateral flap for clockwise rotation. Then if the pilot wants to pitch the nose up a slight roll is generated and the pilot will have to correct with a right or left lateral command for counterclockwise and clockwise rotating blades, respectively.

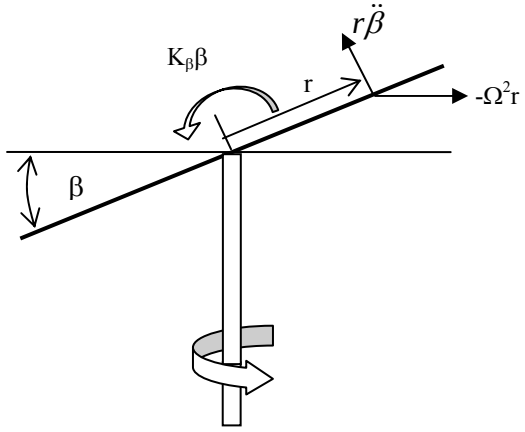

Figure 4.7: Moments responsible for blade flap

Adding aerodynamic and fuselage considerations to the flapping motion brings equation 4.6 to

$$\beta'' + \beta\lambda_b^2 = \frac{2}{\Omega}\left(-p\cos\varphi - q\sin\varphi\right) + \frac{1}{I_\beta\Omega^2}\int_0^R L\left(r,\varphi\right)dr \tag{4.10}$$

Rearranging terms and using a uniform inflow velocity model, the equation is

$$\beta'' + \frac{\gamma}{8}\beta + \lambda_\beta^2\beta = \frac{2}{\Omega}\left(-p\cos\varphi - q\sin\varphi\right) + \frac{\gamma}{8}\left(\theta - \frac{4}{3}\lambda_i + \frac{p}{\Omega}\sin\varphi + \frac{q}{\Omega}\cos\varphi\right) \tag{4.11}$$

where γ is the blade lock number, λ_i is the inflow velocity normalized by ΩR. θ is the applied blade pitch and can be written as

$$\theta = \theta_o + \theta_{1c}\cos\varphi + \theta_{1s}\sin\varphi \tag{4.12}$$

where θ_o is the collective pitch, and θ_{1c} and θ_{1s} the lateral and longitudinal cyclic input respectively. The rotor flapping motion is expressed in a quasi-steady-state form, and if retaining only first harmonic terms of the Fourier Series expansion, β can be written as

$$\beta = \beta_o + \beta_{1c}\cos\varphi + \beta_{1s}\sin\varphi \tag{4.13}$$

The β_0 term is called the blade coning and is a result of the collective pitch. β_{1c} is the longitudinal flapping and β_{1s} is the lateral flapping. Figure 4.8 illustrates this relationship. Substituting the equations 4.12 and 4.13 into equation 4.11, one can collect terms to produce values for longitudinal and lateral flapping

$$\begin{aligned}
\beta_o &= \frac{\gamma}{8\lambda_\beta^2}\left(\theta_o - \frac{4}{3}\lambda_i\right) \\
\beta_{1c} &= \frac{1}{1+S_\beta^2}\left\{S_\beta\theta_{1c} - \theta_{1s} + \left(S_\beta\frac{16}{\gamma} - 1\right)\frac{p}{\Omega} + \left(S_\beta + \frac{16}{\gamma}\right)\frac{q}{\Omega}\right\} \\
\beta_{1s} &= \frac{1}{1+S_\beta^2}\left\{S_\beta\theta_{1s} + \theta_{1c} + \left(S_\beta + \frac{16}{\gamma}\right)\frac{p}{\Omega} - \left(S_\beta\frac{16}{\gamma} - 1\right)\frac{q}{\Omega}\right\} \\
S_\beta &= \frac{8\left(\lambda_\beta^2 - 1\right)}{\gamma}
\end{aligned} \tag{4.14 a-d}$$

Here, S_β is the stiffness number and provides a ratio of hub stiffness to aerodynamic moment. The stiffness number equals 0.43 including hinge offset and 0.23 without, showing the significance hinge offset plays in the blade motion.

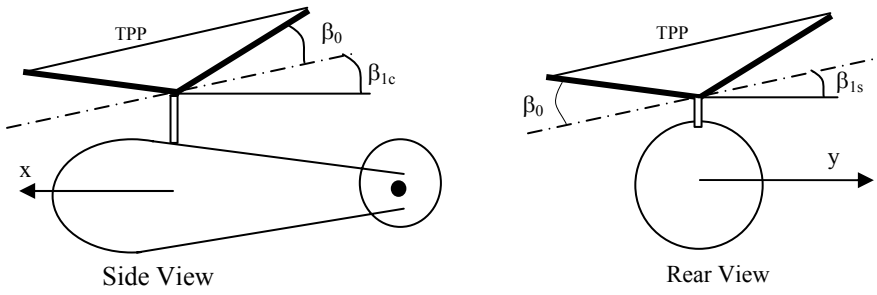

Figure 4.8: Visualization of blade coning and flapping. The flapping angles correlate to tilt of the disc tip path plane

As stated above, a natural frequency greater than one (1) indicates the blades find a new equilibrium position faster than one revolution. The Bergen uses a governor (Futaba GV-1) which maintains head speed at 1500 RPM. The blades then find a new equilibrium position in less than 40 milliseconds. A closer approximation of the required time can be made using the blade time constant, defined as $\tau_M = 16/\gamma\Omega$. The amount of time required for the blade to reach 63% of its response is 19.7 milliseconds. This equates to an azimuth angle of 176 degrees or 3.07 radians. The relatively fast response of the blades compared to the body dynamics justifies a quasi-static assumption in modeling the main rotor.

4.5 Main Rotor

The advent of Sikorsky's success realized many expectations of a rotary wing aircraft. Despite the differences in appearance between a rotary and fixed-wing craft, the fundamental concepts governing flight hold in both cases. A fixed-wing craft uses a fixed airfoil, the wing, to generate lift. Control surfaces on the wing provide controllability and stability. Helicopters employ a number of moving airfoils, rotor blades, which spin uniformly around a fixed rotor shaft. The number of rotor blades can vary but it is usually between two to six. The Bergen Industrial Twin has two main rotor blades and further analysis is based on this configuration.

4.5.1 Thrust Generation

Thrust generated by the blades can be found using a momentum energy method or a blade-element method. Both methods are discussed, beginning with the momentum energy method. This is the simplest method to estimate the thrust produced by a rotor

and makes a number of assumptions, including steady, inviscid, and incompressible flow. It also assumes the velocity distribution along the rotor blade is constant. In essence, the momentum theory uses the conservation laws of mass, energy and momentum. The thrust, T_M, can be written as

$$T_M = 2\rho A_d \left(V_c + v_1\right) v_1 \tag{4.15}$$

where A_d is the rotor disk area, V_c is the vertical velocity, and v_1 is fluid velocity at the disk, called the induced velocity. For a hover condition the thrust is equal to the gross weight of the vehicle, or 32 pounds. The induced velocity is then found to equal 5.28 meters per second.

Blade element theory shares most of the assumptions as momentum theory, except it accounts for the non-uniform inflow velocity distribution. Blade element theory integrates the amount of lift produced by an infinitesimal section of the rotor (δr). Then, the incremental lift is given by

$$\delta L = \frac{1}{2}\rho\left(\Omega r\right)^2 c_l c \delta r \tag{4.16}$$

where c_l is the local lift coefficient, Ω is the rotational speed in radians per second, ρ is the density of air, and c is the blade chord. The local lift coefficient, c_l, can be written as a function of the local angle of attack, α, and slope of the lift curve per radian, a. Prouty reports that conventional airfoils typically have a lift slope curve value of 5.73 per radian. This value is used in the model and produces acceptable results. The local angle of attack, α, can be represented as the difference between the blade pitch angle, θ, and inflow angle, ϕ, as shown in Figure 4.9. The inflow angle is defined as v1/ΩR using the small angle assumption. Making these substitutions for the local lift coefficient brings equation 4.16 to the form

$$\delta L = \frac{1}{2}\rho(\Omega r)^2 a\left(\theta - \frac{v_1}{\Omega r}\right)c\delta r \quad = \quad \frac{\rho}{2}ac\Omega^2 \int_{Ro}^{R}\left(\theta r^2 - \frac{v_1 r}{\Omega}\right)dr \tag{4.17}$$

$$T = bL = \frac{\rho}{2}bac\Omega^2\left\{\frac{\theta}{3}\left(R^3 - Ro^3\right) - \int_{Ro}^{R}\left(\frac{v_1 r}{\Omega}\right)dr\right\} \tag{4.18}$$

where T is the thrust defined as the summed lift of each blade. The induced velocity is expressed as

$$v_1 = \frac{-\left(\frac{\Omega}{2}abc + 4\pi V_c\right) + \sqrt{\left(\frac{\Omega}{2}abc + 4\pi V_c\right)^2 + 8\pi b\Omega^2 acr\left(\theta - \frac{V_c}{\Omega r}\right)}}{8\pi} \tag{4.19}$$

Substituting equation 4.19 into 4.18 and integrating yields a lengthy closed-form solution.

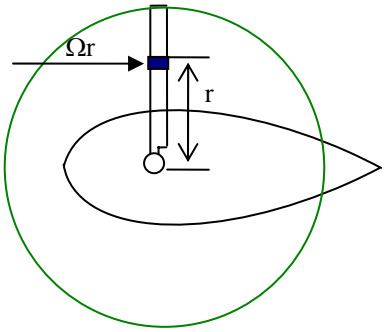

Figure 4.9 (a): Blade element theory

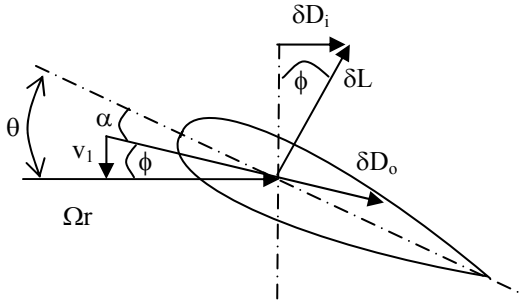

Figure 4.9 (b): Analysis of forces acting on the rotor surface

Equations 4.18 and 4.19 demonstrate that thrust is a factor of the blade geometry and configuration (R, Ro, c, b, a), atmospheric properties (ρ), and operational conditions (θ, Ω, V_c). Assuming constant thrust conditions, the induced velocity and thrust as a function of radial position are shown in Figure 4.10. The following operating conditions are used:

Ω = 1500 RPM

θ = 6.63°

V_c = [0, 3, -3] (m/s)

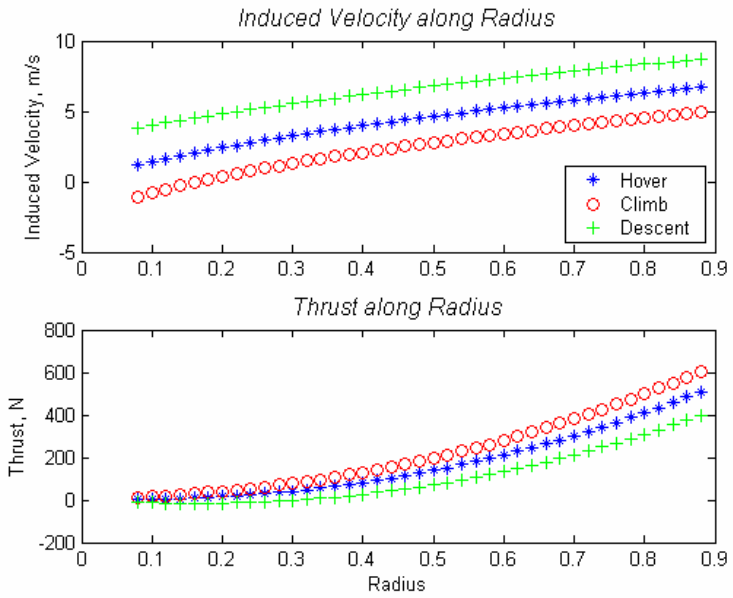

Figure 4.10: Variation of induced velocity and thrust in vertical flight and hover

For steady climb rates, the rotor thrust is close to the hover value with increases accounted for by the augmented vertical drag of the fuselage. The average angle of attack in climb is therefore close to the hover value. The total thrust for hover, climb, and descent is 31.59, 38.86, and 22.85 pounds respectively.

Comparing momentum theory and blade element theory shows that momentum theory sacrifices detail, and a greater physical understanding of conditions at the rotor, for simplicity and quick calculations. The main difference is the shape of the inflow velocity. In an hovering condition, momentum theory estimates an inflow velocity of 5.3 meters per second, while blade element theory predicts an average velocity of 5.025 meters per second and a thrust of 32.6 pounds. However, thrust is the main quantity of interest in control applications and for hovering and climbing flight conditions, momentum theory produces reasonable results. It should be noted that the above analysis only treats vertical flight. Forward flight brings a higher level of complexity into the calculations.

4.5.2 Main Rotor Torque

The torque produced by the main rotor is an important parameter. As in any system torque is equal to a force multiplied by a moment arm. For the rotor blade the drag force and radial section are the variables under consideration. Referencing Figure 4.9 (b) the drag force is composed of an induced drag term, δD_i, and a profile drag term, δD_o. The induced drag is simply the lift component parallel to the relative airspeed equal to $\delta L\phi$ using the small angle assumption. The profile drag can be computed in a similar manner as the lift. The torque is then equal to the sum of these forces multiplied by the radius, or

$$\begin{aligned} \partial Q &= r\left(\partial L\phi + \frac{\rho}{2} c_d c \left(\Omega r\right)^2 \right) \delta r \\ \partial Q &= r\left\{ \frac{1}{2}\rho\left(\Omega r\right)^2 a c_l c\phi\delta r + \frac{1}{2}\rho\left(\Omega r\right)^2 c_d c\delta r \right\} \end{aligned} \tag{4.20}$$

where c_d is the average drag coefficient and Q is the torque. The value of c_d is taken from wind tunnel test data and will be discussed in more detail later. The integration for the total torque is again a long process and can be evaluated numerically or with integration tables.

Momentum theory again offers a simplifying approach. Assuming a uniform induced velocity over the blade, v_{1c} can be written as

$$v_{1c} = -\frac{V_c}{2} + \sqrt{\left(\frac{V_c}{2}\right)^2 + \frac{T}{2\rho A_d}} \tag{4.21}$$

Here v_{1c} is the induced velocity in a hover or climbing condition. The torque can then be expressed as

$$dQ = \frac{ba\rho\Omega c}{2}\int_{Ro}^{R} v_{1c}\theta r^2 - \frac{v_{1c}^2 r}{\Omega}\delta r + \frac{b\rho\Omega^2 cc_d}{2}\int_{Ro}^{R} r^3 \delta r$$

$$Q = \frac{b\rho\Omega c}{2}\left\{a\left(\left(\frac{R^3 - Ro^3}{3}\right)v_{1c}\theta - \frac{v_{1c}^2}{2\Omega}\left(R^2 - Ro^2\right)\right) + \Omega c_d\left(\frac{R^4 - R_o^4}{4}\right)\right\} \tag{4.22}$$

Assuming hovering conditions, the torque calculated with the blade element theory produces a value of 7.7 Newton meters while momentum theory yields a value of 7.3 Newton meters.

4.6 Main Rotor Control

Once the thrust vector is generated, a variety of mechanical linkages are used to direct it, providing longitudinal, lateral, and vertical control. The blades attach to blade grips, which in turn connect to the rotor hub through a bearing assembly. This assembly can be configured as a rigid teetering hub. As the blades rotate around the shaft, a mechanism known as the swash plate changes the blade pitch in either a collective or cyclic manner. The total blade pitch receives contribution from collective and cyclic commands. If the swash plate remains perpendicular to the rotor shaft, collective pitch is induced and commands vertical flight by varying the thrust generated by the rotor. The pitch of the advancing and retreating blades is increased by the same amount, and remains constant throughout each revolution. Cyclic pitch causes the blade's pitch to go through a complete feathering, or sinusoidal, cycle each revolution. Thus, blade pitch varies as a function of the azimuth angle. Cyclic pitch occurs when the swash plate is tilted with respect to the rotor shaft. Figure 4.11 shows the Bergen's swash plate and Figure 4.12 illustrates a schematic illustrating the swash plate's operation.

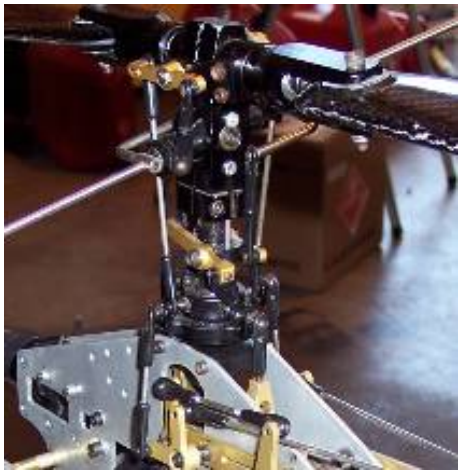

Figure 4.11: The swash plate commands cyclic pitch

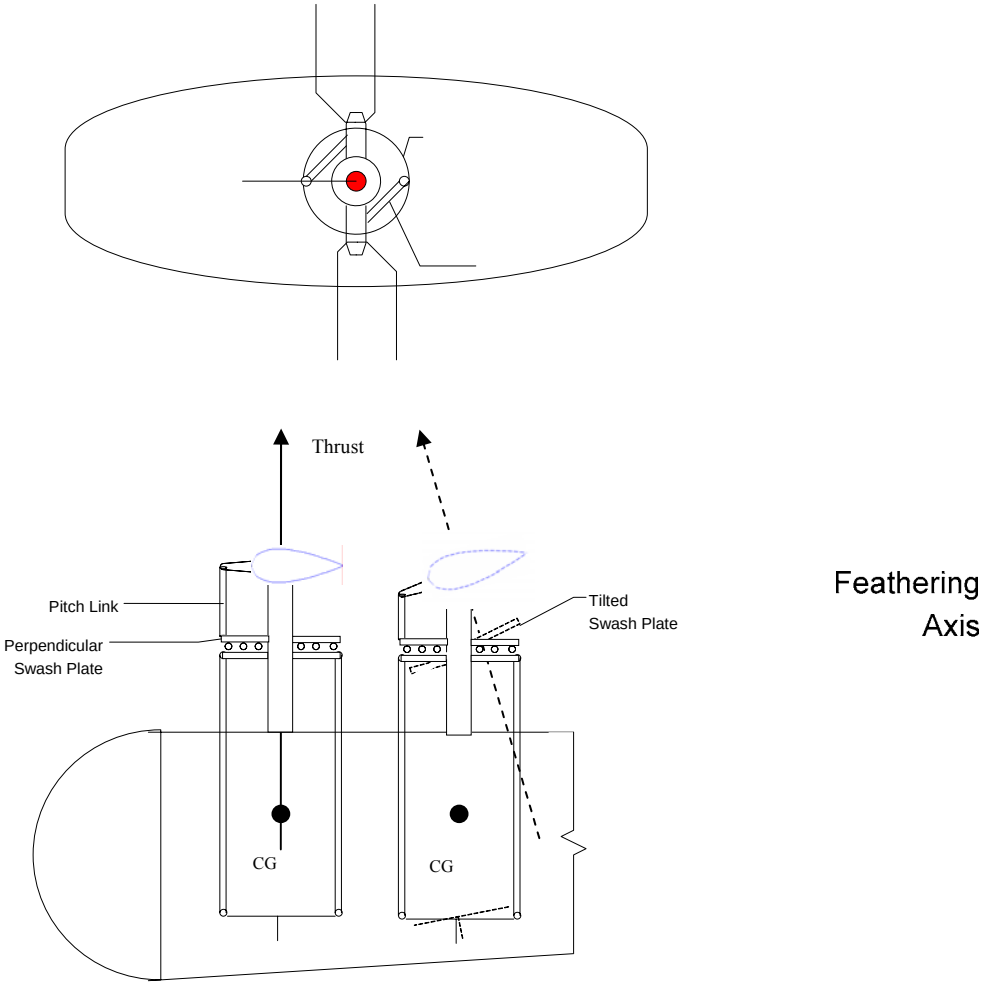

Figure 4.12: Schematic of the swash plate's operation

Because the pitch horn is connected 90° ahead of the blade, tilting the swash plate forward causes the advancing blade to decrease in pitch and the retreating side to increase. When the blade is over the nose or tail, θ is at the nominal value. As the advancing blade's pitch is decreased it will flap down over the nose, while the retreating blade will flap up over the tail. This results in unbalanced moments, effectively pitching the thrust vector, and causing the helicopter to translate forward. The same analysis holds true for lateral and reward translation [1].

4.6.1 Stabilizing Rotor

Due to the increased control sensitivity of small scale helicopters, most designs incorporate a stabilizing rotor, also known as a Bell-Hiller stabilizing bar. From a control

viewpoint, the stabilizing rotor is a dynamic feedback system on pitch and roll rates. The system consists of a combination of Bell and Hiller stabilizing rotors. The Bell system consists of a bar which behaves like a gyro device providing lag damping to the rotor. The Bell bar is pivoted to the rotor shaft with weights on the end and viscous damping. A linkage connects the bar to the blade so that a tilt of the bar relative to the shaft causes a change of blade pitch. The Hiller system is similar to the Bell bar, except that it uses small airfoils on the tips in place to provide viscous damping. The pilot also controls the Hiller bar directly. Combining the two systems results in the configuration shown in Figure 4.13. Here the cyclic inputs commanded by the pilot do not go directly into the blades but are mixed with inputs from the stabilizing rotor [20].

The stabilizing rotor has a teetering head design and does not produce any cross-coupling in the pitch and roll rates. Tischler proposed a first order model to capture the stabilizing rotor dynamics as

$$\begin{aligned} \tau_S \dot{d} &= -d - \tau_S p + D_{lat}\delta_{lat} \\ \tau_S \dot{c} &= -c - \tau_S q + C_{lon}\delta_{lon} \end{aligned} \tag{4.23}$$

where d and c are the stabilizing rotor's lateral and longitudinal flapping angles, respectively. The pilot's cyclic commands δ_{lat} and δ_{lon} are then augmented to produce

$$\begin{aligned} \overline{\delta}_{lat} &= \delta_{lat} + K_d d \\ \overline{\delta}_{long} &= \delta_{lon} + K_c c \end{aligned} \tag{4.24}$$

where K_d and K_c are stabilizer gains and are a function of the geometry. Further details can be found in [21, 22].

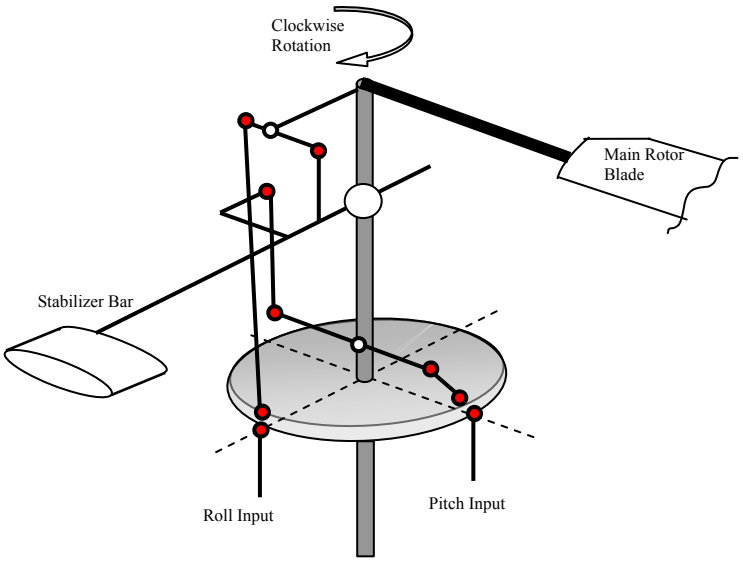

Figure 4.13: Bergen Cyclic Control Scheme with stabilizing rotor

4.7 Airfoil Considerations

As in fixed-wing development, the airfoil's characteristics play an important role in the amount of lift and power required for helicopter flight. Furthermore, the rotor is the source of the dominant forces and moments in the helicopter; therefore, an overview of airfoils is given here. Most scale helicopters, including the one under consideration, use a constant chord, symmetric airfoil. Early investigation of common airfoils resulted in a series of airfoil names produced by the National Advisory Committee for Aeronautics (NACA), the predecessor of NASA. A popular series, is the NACA 4-digit family where the first digit represents the maximum camber (as percent of the chord), the second digit represents the position of maximum camber (as 1/10 the chord), and the last two digits represent the maximum thickness of the airfoil, again normalized by the chord. For example, the NACA 0015 airfoil is a symmetric airfoil with a maximum thickness of 15% the chord. NACA also produced equations representing each airfoil along the ordinate, assuming the chord runs along the x axis from 0 to 1. The representing equation is [17]

$$\pm y = 0.29690\sqrt{x} - 0.12600x - 0.35160x^2 + 0.28430x^3 - 0.10150x^4 \qquad (4.25)$$

Measurements of the Bergen airfoil were taken and compared to a number of symmetric NACA airfoils. Figure 4.14 shows that the airfoil under question agrees with the NACA

0015. This assists in estimating lift and drag coefficients as extensive wind tunnel testing has been performed on the NACA series airfoils.

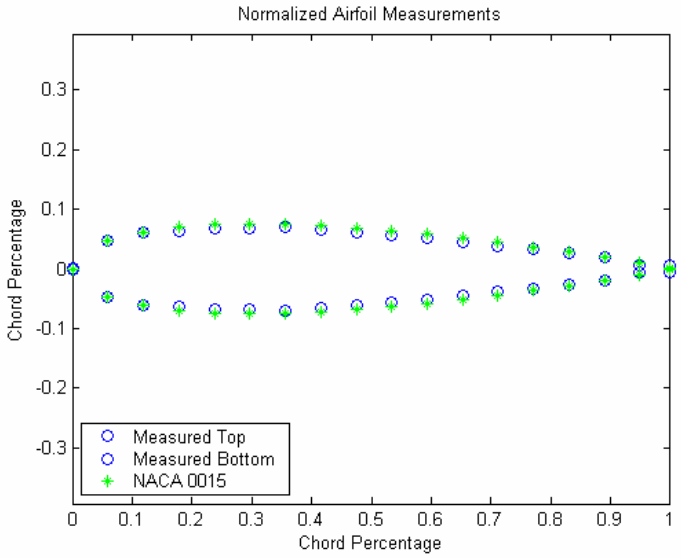

Figure 4.14: Comparison of cross section measurements of the Bergen's main rotor blades and the NACA 0015 airfoil

Wind tunnel testing performed by Sheldahl and Klimas at the Sandia National Laboratories [23] provides lift and drag coefficient values for the NACA 0015 airfoil at various angles of attack and Reynolds Number. The appropriate Reynolds Number for this analysis uses the blade tip speed as the velocity and chord as the dimensional characteristic. Blade speed is controlled by a governor at 1500 RPM. The tip of the blade, including offset, is 0.89 meters, resulting in a tip speed of 140 m/s and a Reynold's Number of 5.481×10^5.

In order to validate these data, payload tests were performed with the Bergen helicopter where the loaded craft was put into a hover by a pilot so as to be out of ground effect. An observer noted the collective stick position. The blade speed was measured using an optical tachometer. After the helicopter was landed the blade pitch was measured with an appropriate device. With fifteen pounds of payload the blade pitch was found to be approximately 6.6 degrees. A program was written that used the wind tunnel lift and drag coefficient data to determine the thrust generated in hovering conditions. A blade pitch of 6.6 degrees results in 33.3 pounds of thrust and a lift coefficient of 0.4897. This

blade pitch value agrees with ground measurements. A second program was written that calculates the thrust produced based on a combined blade-element momentum theory method. Inputting 6.6 degrees as the blade pitch angle, and assuming a lift slope curve value of 5.73 , the resulting thrust is 31.59 pounds with a lift coefficient of 0.4308. These results show the validity of the theoretical formulations when compared to actual flight data.

4.8 Tail Rotor

The tail rotor is primarily responsible for yaw control, producing anti-torque which offsets the main rotor torque for a given flight condition. The tail rotor of the Bergen is modeled in a similar fashion as the main rotor. Tail rotor RPM is assumed constant since it is driven by a torque tube from the main rotor gear. Flapping degrees of freedom are neglected as the tail rotor's response is even faster than the main rotor's and too fast to impact the rigid body forces and moments. Collective input is the only command issued to the tail rotor, directly effecting thrust, induced velocity, and power required. Vertical fin influence is also modeled.

4.9 Fuselage

In reality, the fuselage is responsible for lift and drag. However, the percentage of lift is negligible and the fuselage is modeled as a flat plate effectively limiting translational speed and adding drag in vertical flight. The influence of downwash interaction is also modeled as a pitching moment. Estimating the aerodynamic center and effective flat plate area are the data required for fuselage force and moment calculations. In this study the aerodynamic center is taken to be the geometric center [5].

4.10 Horizontal Fin

The horizontal fin produces lift and drag components important in solving the longitudinal equations, most notably the pitch equation. Effectively, the horizontal fin exerts a stabilizing moment when the helicopter attains sufficient forward speed. The forces and moments produced by the aerodynamic lift and drag are generated as airflow passes over the fin, which becomes very complicated in forward flight when the inflow

and main rotor downwash interact. Thus, the horizontal fin has the most influence in forward flight but still contributes in hover equilibrium.

4.11 Vertical Fin

The vertical fin primarily affects the yawing moment in forward flight. However, the interference of the vertical fin in tail rotor thrust generation is modeled in hover and forward flight.

4.12 Ground Effect

Helicopters flying near ground level require less operating power than when flying high above the ground. This phenomenon is referred to as ground effect and can be visualized in Figure 4.15. Imagine a helicopter hovering near the ground and an image helicopter submersed in the ground the same distance as the real helicopter is above ground. The image helicopter effectively pushes the real helicopter upwards and reduces the power the real helicopter requires to hover. The induced velocity is also reduced by an amount [2]

$$\delta v_1 = \frac{A_d v_1}{16\pi z^2} \tag{4.26}$$

Referring to Figure 4.9 (b) this decreases the induced drag, δD_i. If constant thrust is maintained (i.e., constant angle of attack), then the blade pitch must be reduced. The power required to hover in ground effect is estimated by [19]

$$C_p = C_{p_o} + \kappa_G * \left(C_{p_i}\right)_\infty \tag{4.27}$$

where

$$\kappa_G = \frac{1}{0.9926 + 0.0379\left(D/z\right)^2} \tag{4.28}$$

Ground effect has been found to be negligible when the rotor is more than one diameter (D) above the ground and its effects reduce quickly in forward flight.

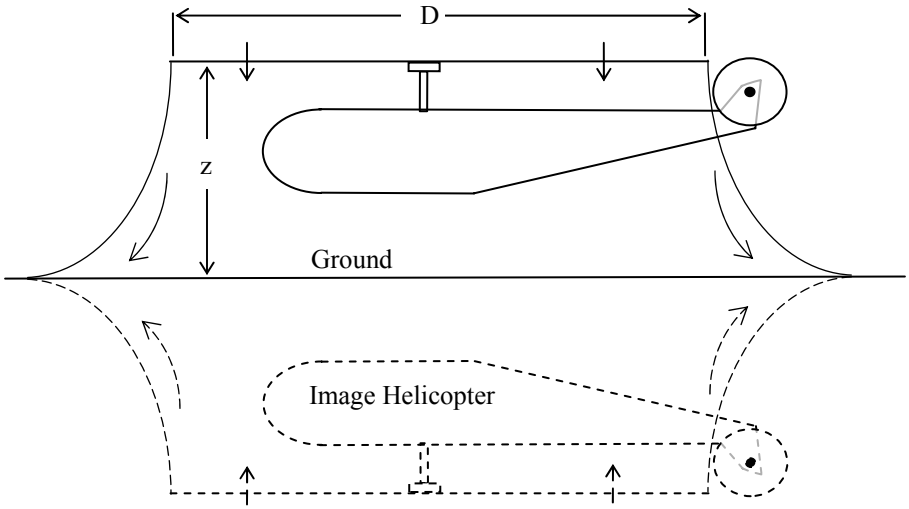

Figure 4.15: Visualization of ground effect

4.13 Required Power

Generally, the power required to perform any maneuver can be isolated into three categories: (1) Induced Power, (2) Parasite Power, and (3) Profile Power. Energy relationships are used to describe these power requirements. One can define a drag value that when combined with the vehicle's speed, represents the total force the vehicle must overcome in order to operate at the given speed. The main rotor is the primary source of required power, but the tail rotor also contributes, especially at higher speeds. Power calculations are similar for both systems.

Induced power can be thought of as the minimum power required to hover, and is expressed as

$$P_{ihov} = Tv_1 \tag{4.29}$$

During forward flight, with the vehicle's speed represented by V, v_1 takes a new form but the induced power equation stays the same

$$v_{in\_FF} = \sqrt{\frac{-V^2}{2} + \sqrt{\left(\frac{V^2}{2}\right)^2 + v_1^4}} \tag{4.30}$$

$$P_i = \frac{Tv_{in\_FF}}{e} \tag{4.31}$$

where e is an efficiency factor estimated to be 0.75 [1].

Parasite power is the power required to overcome the drag of all non-rotor components. The fuselage, landing gear, and avionics box are the elements considered in this analysis. An equivalent flat plate area, f, is used to determine the drag of these components. Essentially, individual components are measured and the total frontal area summed. The parasite power is then written in terms of horsepower as

$$P_p = \frac{f\rho V^3}{1100} \tag{4.32}$$

Profile power arises from the aerodynamic friction the blades experience as they cut through the air. Profile power is expressed as

$$P_{PR} = \frac{\rho A_b (\Omega R)^3 c_d}{550 * 8}\left(1 + 3\mu^2\right) \tag{4.33}$$

where μ is the tip speed ratio, or advance ratio, equal to V/ΩR. Summing each component yields the total power for forward flight. Figure 4.16 shows each component for the main rotor and the total power of the tail rotor.

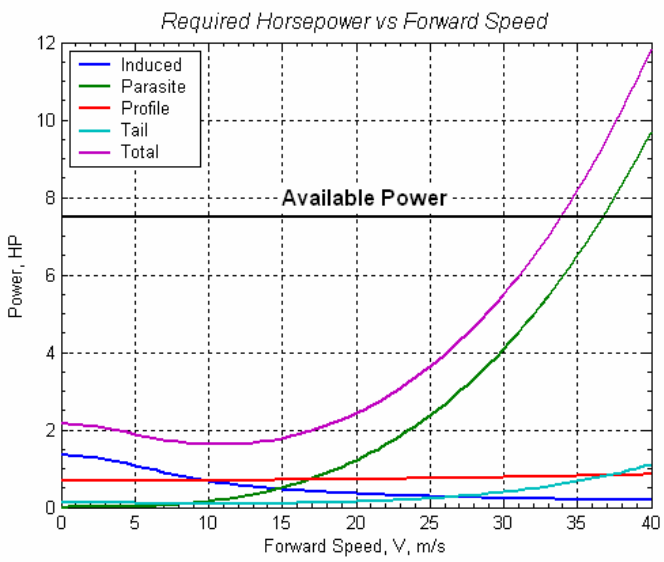

Figure 4.16: Power breakdown at varying forward velocities

As expected, induced power is the main contribution at lower speed while parasite power dominates at higher speeds. Hovering requires approximately 2.15 horsepower for the instrumented Bergen. The minimum power occurs at 10.5 meters per second, or 23.5 miles per hour, consuming 1.5 horsepower. From a power standpoint, the maximum speed attainable in level forward flight is 34 meters per second or 76 miles per hour.

Chapter 5 Trim and Stability Analysis

This chapter analyzes the hover trim condition and stability of the modeled Bergen helicopter. The trim analysis is performed on the six DOF nonlinear model and uses a Newton-Rhapson method to solve system of equations represented in equation 4.4. The unknowns in the equations are main rotor thrust, fuselage pitch angle, longitudinal blade flap constant, tail rotor thrust, fuselage roll angle, and lateral blade flap constant. The stability analysis is performed on a linearized system at the hover condition.

5.1 Trim Conditions

In a trimmed condition, the aircraft is in steady flight and all accelerations, both linear and angular, are zero. Thus, all terms on the right hand side of the force and moment equations are zero except for inertial contributions. Flight conditions such as speed, slide slip angle, climbing angle and rate all contribute to the trimmed flight values. For the special case of hover all aerodynamic contributions of the airframe can be neglected except for the vertical drag of the fuselage and horizontal stabilizer. The longitudinal and lateral dynamics can be decoupled with minimal loss of accuracy. The longitudinal dynamics are incorporated in the X, Z, and M equations as

$$\begin{aligned} X_M &= GW\sin\Theta \\ Z_M + Z_H + Z_F &= -GW\cos\Theta \\ M_M - X_M h_M + Z_M l_M + M_T + Z_H l_H + Z_F l_F &= 0 \end{aligned} \qquad \text{(5.1 a-c)}$$

These equations are easily solved for main rotor thrust, fuselage pitch angle, and longitudinal blade flap coefficient. In a similar fashion the Y, R, and N equations represent the lateral dynamics and provide values for tail rotor thrust, fuselage roll angle, and lateral blade flap coefficient. Recalling the negation of terms including l_m and l_f the Bergen has the following trim conditions in hover

Table 5.1: Trim Values in hover

Thrust (mr) T(M)	Pitch Angle Θ	Longitudinal Blade Flap Constant β1c	Thrust (tr) T(T)	Roll Angle Φ	Lateral Blade Flap Constant β1s
33.8	2	-2	-1.9	3.1	-0.37

The longitudinal flap coefficient is much larger than the lateral flap coefficient. This is explained by the location of the CG relative to the main rotor shaft, which creates a positive pitching moment. In trim analysis, the flapping coefficients produce pitching and rolling moments about the rotor hub to balance any unbalanced moments produced by aircraft configuration, hence, the relatively large a1s value.

In translational flight, one can again decouple the longitudinal and lateral dynamics with a minimal loss of accuracy; however, they remain coupled here. Simulating a level, forward flight condition of 15 meters per second results in the following trim conditions

Table 5.2: Trim Values for forward flight (u=15 m/s)

Thrust (mr) T(M)	Pitch Angle Θ	Longitudinal Blade Flap Constant β1c	Thrust (tr) T(T)	Roll Angle Φ	Lateral Blade Flap Constant β1s
32.8	-6.6	-1.8	-1.8	2.8	0.23

With these values determined, the blade flapping angle can be plotted as a function of the azimuth as depicted in Figure 5.1.

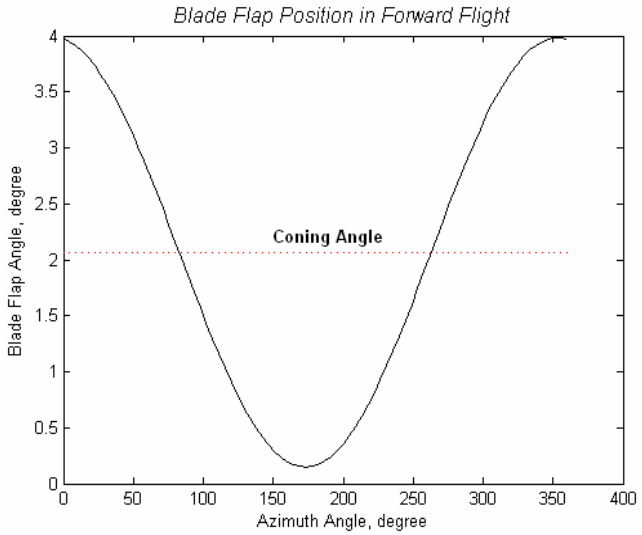

Figure 5.1: Blade flap angle as it rotates

5.2 Stability

The helicopter dynamics are represented by equation 4.3 and take the general form

$$\dot{x} = f(x,u)$$

where **x** is the state vector and **u** the command vector. For linear control it is necessary to linearize the dynamics about some trimmed flight condition. Moreover a greater physical appreciation of helicopter dynamics is gained when linearization is performed. Typically, the flight condition is represented by the vector [V, β_{ss}, γ_c]. Here V is the flight airspeed, β_{ss} the sideslip angle, and γ_c the angle of climb or descent. Hover is the trimmed condition in this study. The linearized system then takes the form

$$\dot{x} = Ax + Bu$$

where

$$\mathbf{x} = \{u\ v\ p\ q\ \Phi\ \Theta\ w\ r\ \}$$

and

$$\mathbf{u} = \{\delta_{lat}\ \delta_{lon}\ \delta_{tr}\ \delta_{coll}\}$$

The A matrix compromises the linear dynamics and is composed of stability derivatives, which represent the change in forces and moments when perturbed by the states. In other words A is the Jacobian

$$\frac{\partial \begin{bmatrix} F \\ M \end{bmatrix}}{\partial x}_{x=xtrim}$$

and B is

$$\frac{\partial \begin{bmatrix} F \\ M \end{bmatrix}}{\partial u}_{u=utrim}$$

The stability derivative $\partial X/\partial u$ represents the change in X when perturbed by u. Typically the force derivatives are normalized by the vehicle mass and the compact notation results, X_u. The rotational forces are normalized by the appropriate moment of inertia; for example, $R_w = \frac{\partial R}{\partial w}\frac{1}{I_{xx}}$. A number of methods are available in calculating the stability derivatives, including analytical differentiation or correlation with flight data. Prouty

presents a method combining differentiation with charts produced from flight data and this methodology is employed here. The resulting A and B matrices take the form

$$A = \begin{bmatrix} X_u & X_v & X_p & X_q & 0 & -g\cos\theta & X_w & X_r \\ Y_u & Y_v & Y_p & Y_q & g\cos\theta\cos\phi & -g\sin\theta\sin\phi & Y_w & Y_r \\ R_u & R_v & R_p & R_q & 0 & 0 & R_w & R_r \\ M_u & M_v & M_p & M_q & 0 & 0 & M_w & M_r \\ 0 & 0 & 1 & \sin\phi\tan\theta & 0 & 0 & 0 & \cos\phi\tan\theta \\ 0 & 0 & 0 & \cos\phi & 0 & 0 & 0 & -\sin\phi \\ Z_u & Z_v & Z_p & Z_q & -g\sin\phi\cos\theta & -g\sin\theta\cos\phi & Z_w & Z_r \\ N_u & N_v & N_p & N_q & 0 & 0 & N_w & N_r \end{bmatrix} \quad (5.2)$$

$$B = \begin{bmatrix} X_{lat} & X_{lon} & 0 & X_{coll} \\ Y_{lat} & Y_{lon} & Y_{tr} & Y_{coll} \\ R_{lat} & R_{lon} & R_{tr} & R_{coll} \\ M_{lat} & M_{lon} & M_{tr} & M_{coll} \\ 0 & 0 & 0 & 0 \\ 0 & 0 & 0 & 0 \\ 0 & 0 & 0 & Z_{coll} \\ 0 & 0 & N_{tr} & N_{coll} \end{bmatrix} \quad (5.3)$$

The dynamics are described by equation 5.2 and the inputs by 5.3. Note that the 11 DOF analytical model will retain a similar structure but some of the stability derivatives will change. See Appendix B for the model structure and [8] for further details.

Solving for the eigenvalues of the unforced linear system results in the open-loop pole-zero map, this can be used to characterize the stability of the nonlinear system for small motions about the trimmed point. The eigenvalues for the Bergen in an hovering condition are shown in Figure 5.2.

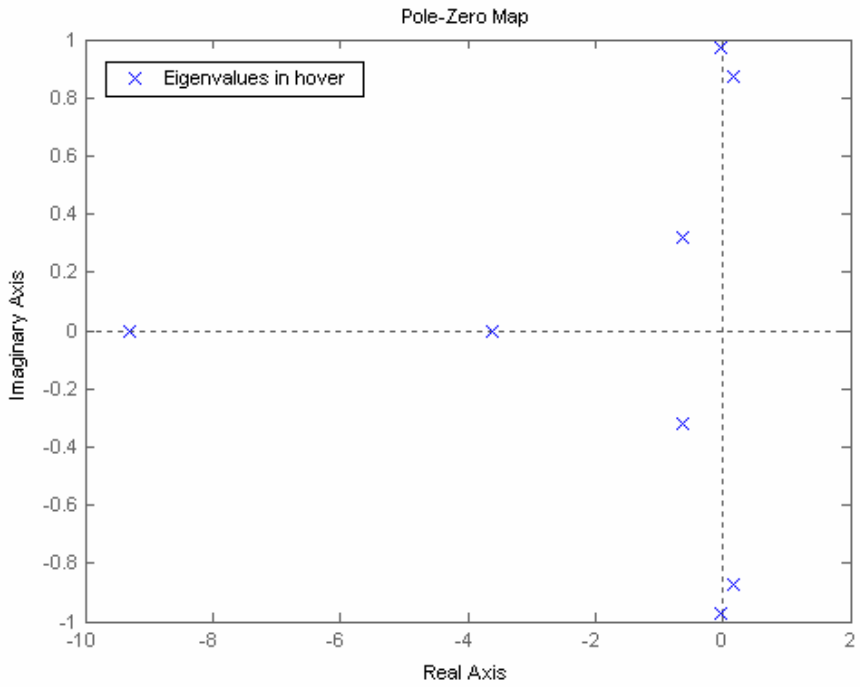

Figure 5.2: Modes for the hovering condition

Two pairs of unstable or marginally stable complex poles exist. In order to identify these modes, the longitudinal and lateral dynamics are decoupled and analyzed separately as was done in trim analysis. The unforced longitudinal dynamics are given as

$$\begin{Bmatrix} \dot{u} \\ \dot{w} \\ \dot{q} \\ \dot{\Theta} \end{Bmatrix} = \begin{bmatrix} X_u & 0 & X_q & -g\cos\Theta \\ 0 & Z_w & 0 & -g\sin\Theta \\ M_u & 0 & M_q & 0 \\ 0 & 0 & 1 & 0 \end{bmatrix} \begin{Bmatrix} u \\ w \\ q \\ \Theta \end{Bmatrix} \tag{5.4}$$

The longitudinal motion consists of a low frequency phugoid oscillation, pitch subsidence, and heave subsidence. Solving for the eigenvalues of the longitudinal motion results in

Table 5.3: Calculated Longitudinal Eigenvalues

Longitudinal Eigenvalues	Description
0.1062 ± 0.865i	Unstable phugoid mode
-3.5206	Damped pitch mode
-0.5876	Damped heave mode

Similarly, the uncoupled lateral dynamics are described by

$$\begin{Bmatrix} \dot{v} \\ \dot{p} \\ \dot{r} \\ \dot{\phi} \end{Bmatrix} = \begin{bmatrix} Y_v & Y_p & Yr & g \\ R_v & R_p & 0 & 0 \\ N_v & N_p & N_r & 0 \\ 0 & 1 & 0 & 0 \end{bmatrix} \begin{Bmatrix} v \\ p \\ r \\ \phi \end{Bmatrix} \tag{5.5}$$

The lateral modes consist of the Dutch roll oscillation, roll subsidence, and yaw subsidence [2]. Solving for the lateral eigenvalues yields the following values and description shown in Table 5.4.

Table 5.4: Calculated Lateral Eigenvalues

Lateral Eigenvalues	Description
0.0393 ± 0.9739i	Dutch roll
-0.6687	spiral subsidence
-9.2925	roll subsidence

From these determinants the coupled modes are identified in Table 5.5.

Table 5.5: Identification of coupled modes

Coupled Eigenvalues	Description
-0.626 ± 0.319i	Yaw-heave oscillation
0.162 ± 0.87i	Unstable phugoid
-0.0222 ± 0.969i	Dutch Roll
-3.61	Pitch subsidence
-9.31	Roll subsidence

Comparison of the coupled and decoupled modes is shown in Figure 5.3. Most of the modes are similar with the exception of the coupled yaw-heave oscillation which takes the form of two first order systems in the uncoupled case. A majority of this coupling is

seen in the yaw response to a collective input arising from the increased torque produced by the main rotor blades. This coupling is illustrated in Appendix C.

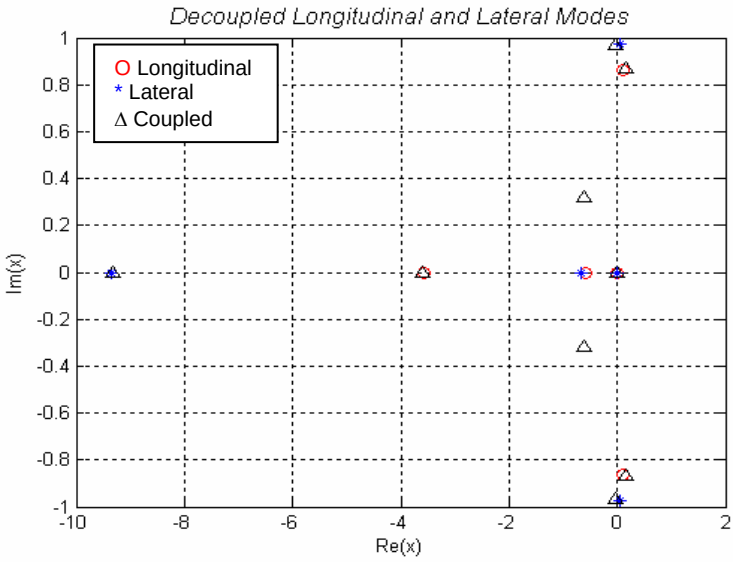

Figure 5.3: Comparison of coupled and decoupled modes

5.3 Response in Hover

This subsection briefly discusses the vertical, yaw, and cyclic responses to step inputs of the appropriate channel. All of the responses match well with established theory. As expected from the analysis in 5.2, the vertical and yaw dynamics are inherently stable while the pitch and roll axis are unstable.

5.3.1 Vertical Response

Using the quasi-static assumption for the main rotor the vertical dynamics are described by

$$\begin{aligned} m\ddot{z}_b &= -\gamma \frac{2C_T}{\sigma a} = m\left(Z_{\theta_o}\theta_o + Z_w \dot{z}_b\right) \rightarrow \\ \dot{w} - Z_w w &= Z_{\theta_o}\theta_o \end{aligned} \tag{5.6}$$

Thus, the vertical dynamics are inherently stable and modeled as a first order system with time constant equal to Z_w. A step response reveals the stability of the vertical dynamics.

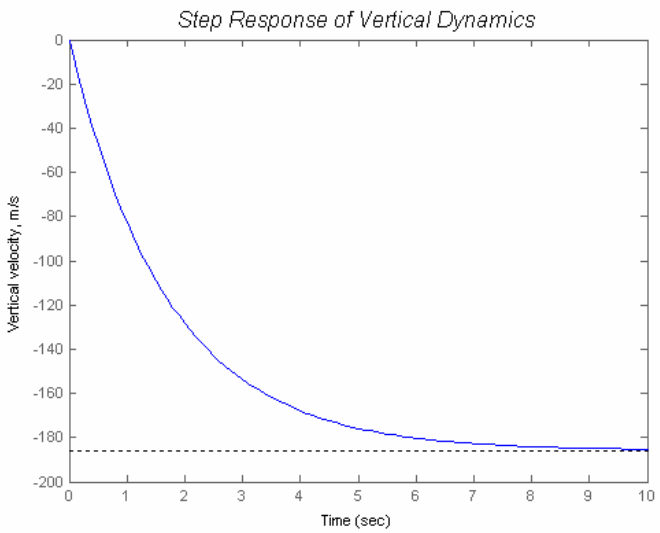

Figure 5.4: Vertical response to collective step input

5.3.2 Yaw Dynamics

The yaw dynamics are also inherently stable and follow a first order system approximated by

$$I_{zz}\ddot{\psi}_b = -\gamma l_T \left(N_r \dot{\psi}_b + N_{\theta T}\theta_{oT} \right) \rightarrow \\ \dot{r}_b - N_r r = N_{\theta T}\theta_{oT} \tag{5.7}$$

The response to a step input in hover is

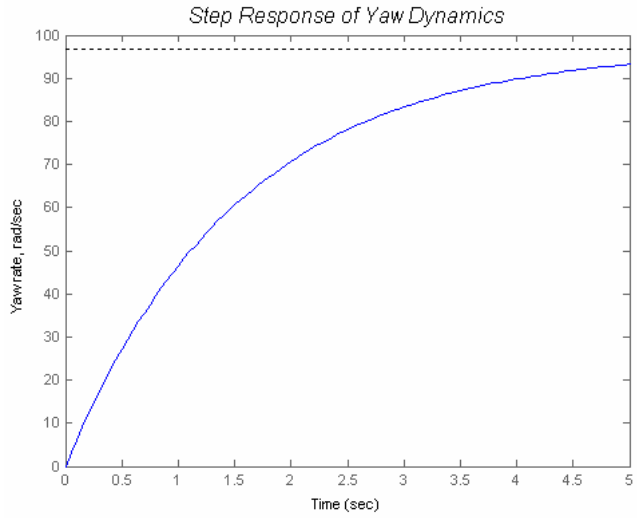

Figure 5.5: Yaw response to a step pedal input

5.3.3 Roll and Pitch Response to Cyclic Inputs

As suggested by the Phugoid and Dutch roll modes, the roll and pitch responses to cyclic commands are coupled and unstable, behaving as a second order system. Thus, a lateral command will provide a response in the roll rate, p, and pitch rate, q.

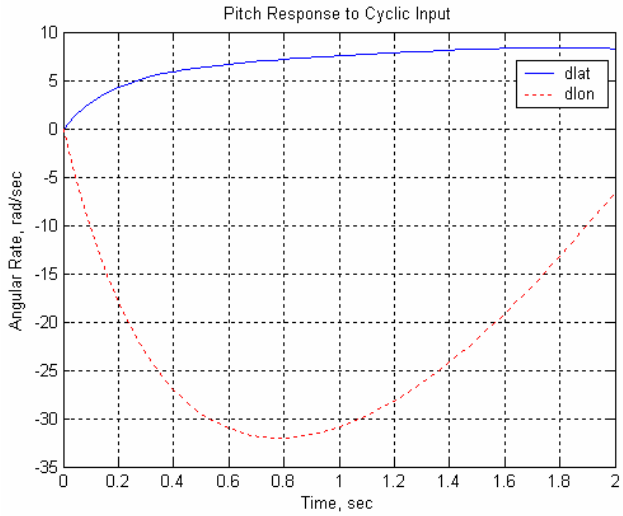

Figure 5.6 (a): Pitch Response

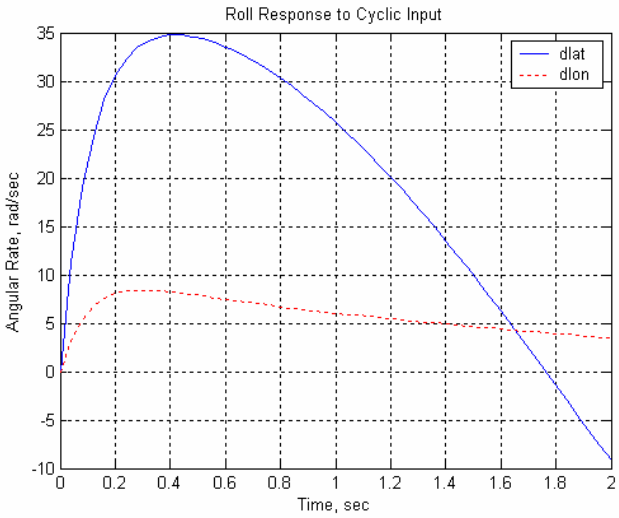

Figure 5.6 (b): Roll Response

A complete display of responses for each input is provided in Appendix C.

Chapter 6 Test Procedure for System Identification

This chapter provides an overview of the CIFER facility. In essence, CIFER is a system identification package which extracts linear models at various flight conditions. The correct test input is critical in developing an accurate linear model since the system under consideration is highly nonlinear. A brief review of accepted inputs is discussed.

6.1 Input Commands

Recent applications of system identification techniques to rotorcraft research have witnessed a number of test inputs including the doublet, "3-2-1-1", and frequency sweep technique. The advantages and draw backs of each method are presented shortly. Separate data should be collected for model creation and model verification. Each method provides certain advantages over another such as ease of testing, identifiable parameters from the input, and the range of frequencies excited. The frequency range of interest, safety, and localized flight are the main factors influencing which method should be used. For parameter estimation from flight data, the modes of the system's dynamics must be excited sufficiently to provide the required data. Also, for an accurate estimation technique the input command must show good correlation between the input and output pairs or show good frequency content. This correlation is of particular importance because the parameter estimation technique applied here focuses on extracting linear models of a highly non-linear system. In order for the linearized model to obtain a high coherence the aircraft must maintain as close as possible to the trim condition during testing [3],[16]. A summary of each technique is presented.

The doublet is a mature method commonly used for fixed-wing aircraft testing. Due to the coupled nature of the helicopter's dynamics, the doublet is not well suited for capturing frequency content but will be used for model verification purposes. An example of the doublet input is illustrated in Figure 6.1.

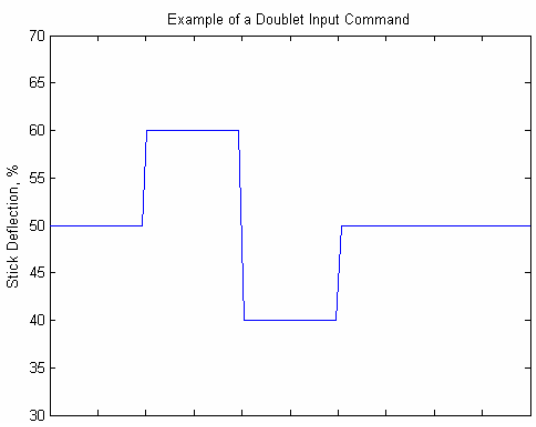

Figure 6.1: Example of the doublet input

The "3-2-1-1" command has been successfully used with rotorcraft. The numbers in the name refer to time intervals between control reversals. For example, the pilot would hold the first position from trim for 3 time units and then reverse the input for 2 time units, etc. An example of this input is shown in Figure 6.2. This input provides data over a broader frequency range than the doublet, but experience has shown it does not allow sufficient time to collect data, or may require the pilot to intervene with large off-axis corrections [3].

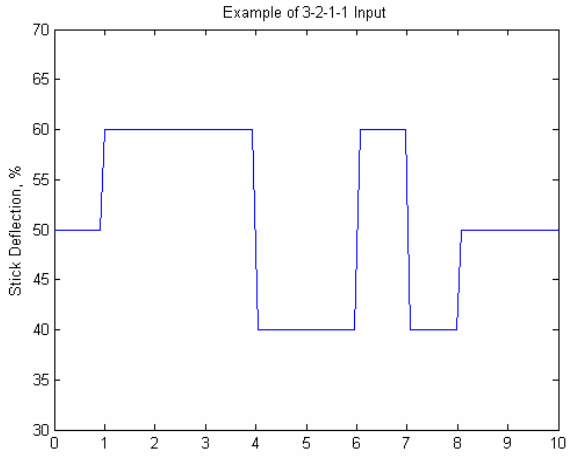

Figure 6.2: Example of the 3-2-1-1 input

The 'frequency sweep' is the third common input and was developed by Tischler. This method calls for the pilot to oscillate an individual input in a sinusoidal fashion starting with a low frequency and increasing until the dynamics in the frequency range of interest have been collected. A frequency sweep input is shown in Figure 6.3 [9]. The amplitude

should be as small as possible while continuous control movement is observed. At low and high oscillations the amplitude is attenuated to maintain the trim condition and reduce the amount of off-axis corrections required. Coupled responses should not be suppressed by the pilot, but if needed to maintain control short, intermittent corrections are acceptable. In general, off-axis corrections should be short steps, or pulses, so as to be uncorrelated with the test data [9].

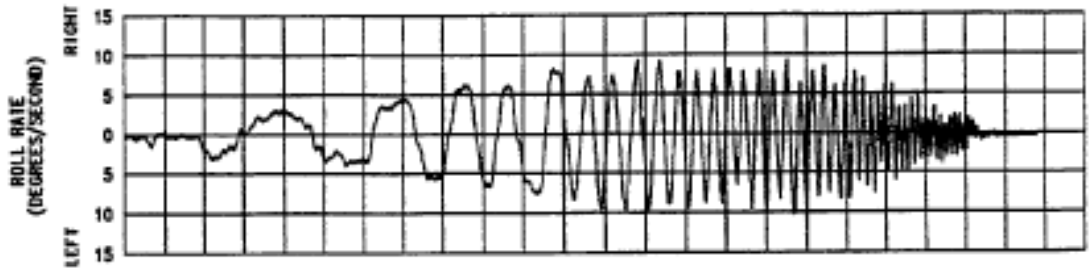

Figure 6.3: Example of the frequency sweep

Members of the Advisory Group for Aerospace Research and Development (AGARD) have experimented with each test method and have collected a database of vehicles and their response to each input. Figure 6.4 shows, in the frequency domain, the effect of each input on the identification process for a BO 105 helicopter. The input autospectrum, magnitude, phase, and coherence are compared. A flat input autospectrum is desired for system identification purposes because it indicates broad system excitation. The coherence function may be defined as a measure of the linearity of a system at individual frequencies, or in other words, the ratio of the output spectrum which can be linearly related with the input spectrum. The coherence function is defined as

$$\gamma_{xy}^2 = \frac{\left|G_{xy}\right|^2}{\left|G_{xx}\right|\left|G_{yy}\right|} \tag{6.1}$$

where G_{xx} is the average input autospectral density, G_{xy} the average cross spectral density, and G_{yy} the average output autospectral density. A coherence of 1 indicates a perfectly linear system at all frequencies. In practice, a coherence value of 0.6 has provided robust linear models [16].

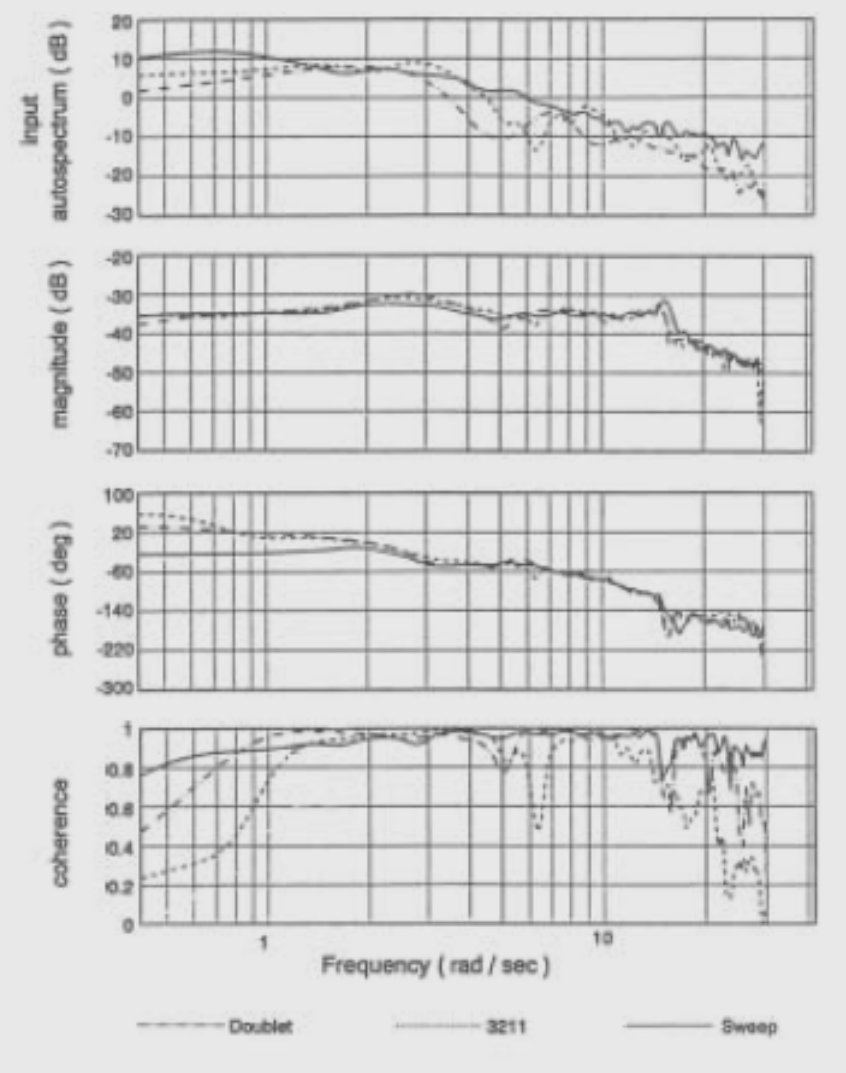

Figure 6.4: Correlation results using the different input techniques

Inspection of Figure 6.4 shows the superior performance of the frequency sweep technique. The coherence has a substantially higher value in the low and high frequency range where significant coupling effects exist. There is also a lower phase in the lower frequency range. For these reasons the frequency sweep is chosen as the test method to collect data for model creation. Doublets are used to collect data for model verification only.

6.2 Test Preparation

In order to perform a safe and successful test, appropriate preparation is required. A timer should be used to indicate to the pilot when the maximum input deflection should occur. One possible approach is to record tones at appropriate frequencies (slow and then

gradually increasing) and play back these tones for the pilot during testing. The pilot should also be alerted to not dwell at the helicopter's natural modes. In most cases this can be visually detected.

6.3 Test Procedure

The pilot has four control inputs, namely, the collective, yaw, longitudinal cyclic, and lateral cyclic. Using the frequency sweep technique, the pilot commands one input per test for duration of approximately 30 seconds. At least three tests providing reasonable data should be conducted for each input. It is expected that three different trim conditions will be tested: (1) hover, (2) forward flight between 1-5 m/s, (3) forward flight between 5-15 m/s. A total of 36 tests with good correlation content should be conducted.

6.4 Data Measurement & Analysis

Due to the short timeframe the AAVT had to develop an autonomous vehicle, a commercially available flight controller was purchased from Rotomotion, LLC. Because the flight controller already enlists the sensors required for modeling purposes, i.e. accelerometers and gyroscopes, it was decided to use this unit as a sensor board for collecting flight data. The following data should be measured [3]:

- control inputs
- translational accelerations and velocities (numerically integrated from acceleration data) for all 3 axes
- rotational rates for all 3 axes as well as roll and pitch attitudes, heading
- rotational accelerations (derived numerically from angular rates).

Proper filtering and error checking should be performed with the collected data and is discussed in [3].

The problem of system identification is complex and requires knowledge from a number of disciplines. System identification techniques have been available to the fixed-wing community for some time, but the complex coupling nature and unstable dynamics of

rotorcraft have disrupted identification techniques until recently. A system identification software package developed jointly by U.S. Army/NASA and Sterling Federal Systems was recently made available to Virginia Polytechnic Institute. The Comprehensive Identification from FrEquency Responses (CIFER) is a mature and proven technology which has computed models for aircraft ranging from rotorcraft to tilt-rotor aircraft [8].

The CIFER methodology is common to the system identification problem. First, a set of input-output test data must be collected. Following the data collection, a nonlinear search for a state space model is performed which matches the input-output frequency response data. The key steps in this process include [8]

- Elimination of uncorrelated noise sources via frequency response calculation
- Fitting each identified frequency response in the region of highest accuracy
- Weighting fit errors based on frequency response accuracy
- Linear analysis to extract parameter accuracy metrics (Cramer Rao bound, coherence)
- Use of confidence ellipsoid theory for multiple correlation evaluations
- Identification and model structure creation
- Fitting responses only in the frequency range where the model structure is appropriate.

The output of the analysis is a state space linear model which accounts for rotor-flap/body coupling and lead-lag dynamics. In the case of small scale rotorcraft, the identification of the stabilizing rotor dynamics is also achieved. Figure 6.5 outlines the identification procedure adopted by CIFER. A detailed explanation of the CIFER process is available in [8] and [9].

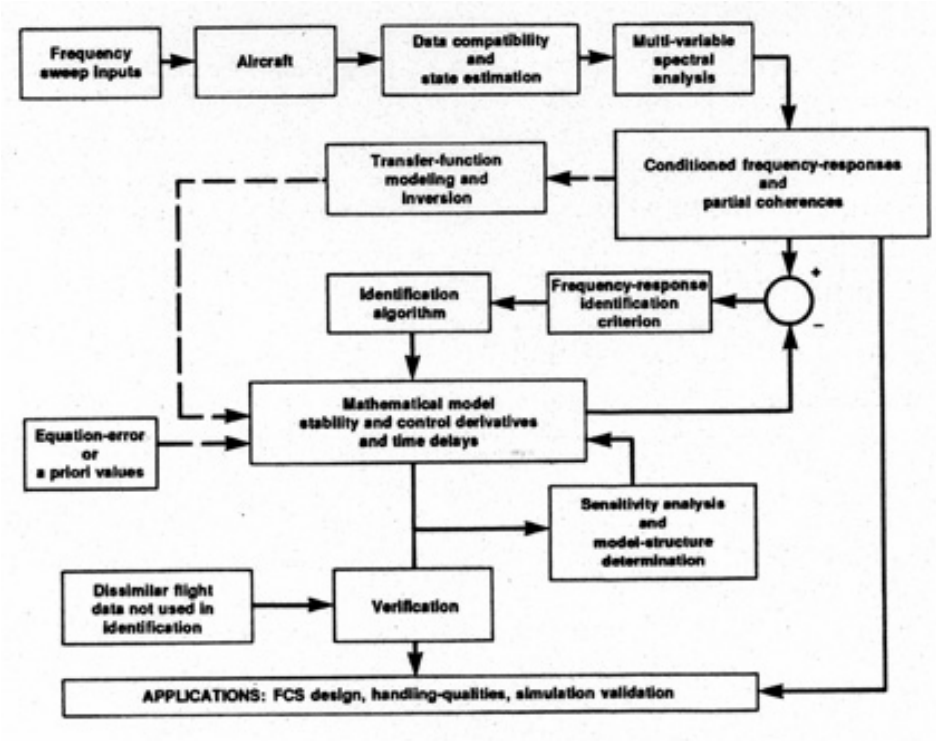

Figure 6.5: Flowchart of the CIFER process

Chapter 7 Conclusions and Future Work

A full six degree-of-freedom theoretical model is developed for the Bergen Industrial Twin experimental helicopter. Careful attention is given to the underlying theory involved. When appropriate, performance calculations, such as required power, are included to help identify efficient flight conditions. A methodical review of each component's contribution to the overall helicopter dynamics is considered and leads to the full nonlinear system dynamics. These equations have as inputs the four pilot's controls and are suitable for simulation. The nonlinear equations are solved for different trim conditions, including hover and forward flight. The trim results are used to linearize the nonlinear model about a hover condition from which analysis of stability and control around the trim condition is possible. The modes of motion for the linearized model are identified and match well with established theory.

The developed model provides a basis for researchers at Virginia Tech to continue work in the field of rotary autonomous aerial vehicles. Future work at Virginia Tech includes controller and obstacle avoidance algorithm development, autonomous heterogeneous and teaming capabilities, as well as continued vehicle modeling. Model validation with flight data is perhaps the most critical task remaining. A majority of this work was performed after a laboratory accident destroyed the Bergen helicopter and a replacement was not obtained in time to be included in this work. Once the new platform arrives, flight data can be collected and compared to the simulated response. Furthermore, the hybrid 11 DOF model can also be obtained once the new platform arrives with the CIFER facility. This will allow development of high bandwidth control systems and provide a more detailed description of the dynamics of the helicopter system.

References

[1] R.W. Prouty, *Helicopter Performance, Stability and Control*, Krieger Publishing Company, 1995.

[2] Gareth D. Padfield, *Helicopter Flight Dynamics: The Theory and Application of Flying Qualities and Simulation Modeling*, AIAA Education Series, 1996

[3] Peter G. Hamel, *Rotorcraft System Identification*, Advisory Group for Aerospace Research and Development, Advisory Report 280, 1991

[4] Alfred Gessow, Garry C. Myers, Jr., *Aerodynamics of the Helicopter*, College Park Press, Republished 1999

[5] Robert K. Heffley, Marc A. Mnich, *Minimum Complexity Helicopter Simulation Math Model*, NASA CR 177476, USAAVSCOM TR 87-A-7, Ames Research Center, 1988

[6] Peter D. Talbot, Bruce E. Tinling, William A. Decker, Robert T. N. Chen, *A Mathematical Model of a Single Main Rotor Helicopter for Piloted Simulation*, NASA TM 84281, Ames Research Center, 1982

[7] Jay A. Farrell , Matthew Barth, *The Global Positioning System and Inertial Navigation*, McGraw-Hill Companies, Inc., 1999

[8] Mark. B. Tischler, Mavis G. Cauffman, *Frequency-Response Method for Rotorcraft System Identification: Flight Applications to BO-105 Coupled Fuselage/Rotor Dynamics*, Journal of the American Helicopter Society, Vol 37, No. 3, pg 3-17, July, 1992.

[9] Mark B. Tischler, Jeffrey N. Williams, Johnnie A. Ham, *Flight Test Manual: Rotorcraft Frequency Domain Flight Testing*, AQTD Project No. 93-14, U.S. Army Aviation Technical Test Center, September 1995

[10] J. Gordan Leishman, *Principles of Helicopter Aerodynamics*, 2000 Cambridge University Press

[11] Averil B. Chatfield, *Fundamentals of High Accuracy Inertial Navigation*, AIAA, 1997

[12] Jay W. Fletcher, *Obtaining Consistent Models of Helicopter Flight-Data Measurement Errors using Kinematc-Compatibility and State Reconstruction Methods*, 46th Annual Forum of the American Helicopter Society, May 1990

[13] Jared Cooper, Shane Barnett, Robert Hartley, *Development of an Autonomous Aerial Research Platform at Virginia Tech*, Virginia Tech Internal Report, 2005

[14] Ferdinand P. Beer, E. Russell Johnston, Jr., *Mechanics of Engineers: Statics and Dynamics*, McGraw-Hill Book Company, 1987

[15] http://www.mne.psu.edu/undergrad/CaseStudy/ME50/TorsionalPendulum/casestudy.html#N4000A0

[16] Robert K. Otnes, Loren Enochson, *Applied Time Series Analysis: Volume 1*, John Wiley and Sons, 1978

[17] Eastman N. Jacobs, Kenneth E. Ward, Robert M. Pinkerton, *The Characteristics of 78 Related Airfoil Section from Tests in the Variable-Density Wind Tunnel*, NACA RN 460

[18] John K. Ziemer, *Pulsed Plasma Propulsion for a Small Satellite – Mission COMPASS P3POINT*, AIAA, ASME, SAE and ASEE, Joint Propulsion Conference and Exhibition, 32nd, Lake Buena Vista, Fl, July 1-3, 1996

[19] Wayne Johnson, *Helicopter Theory*, Princeton University Press, 1980

[20] A.R.S Bramwell, *Helicopter Dynamics*, Edward Arnold Publishers Ltd., 1976

[21] R. Cunha, C. Silvestre, *Dynamic Modeling and Stability Analysis of Model-Scale Helicopters with Bell-Hiller Stabilizing Bar*, AIAA Guidance, Navigation, and Control Conference and Exhibit, August 2003

[22] Bernard Mettler, Mark B. Tischler, Takeo Kanade, *System Identification Modeling of a Small-Scale Unmanned Rotorcraft for Flight Control Design*, Journal of the American Helicopter Society, January 2002

[23] Robert E. Sheldahl, Paul C. Klimes, *Aerodynamic Characteristics of Seven Symmetrical Airfoil Sections Through 180—Degree Angle of Attack for Use in Aerodynamic Analysis of Vertical Axis Wind Turbines*, Sandia National Laboratories, SAND80-2114

Appendix A: Experimental Determination of Center of Gravity and Moment of Inertia Tensor

Center of Gravity

The center of gravity for all three axes was found using two scales. In essence, the center of gravity of any object can be found by the formula

$$\bar{x} * W_{total} = d1 * W1 + d2 * W2 \qquad \text{A1}$$

where W_{total} is the total weight of the object, d1 is the distance from a reference point to the first measurement point, and W1 is the weight measurement at the first point. The same notation follows for d2 and W2. Figures A1-A3 illustrates this process for the Y,X and Z axis respectively. Note that the center of gravity of the modified platform was found. The CAD drawings are only meant to illustrate the process.

$$\bar{y} W_{total} = d * (W1 + W2)$$

$$\bar{y} * 32 = 14.5 * 16 - 14.5 * 16$$

$$\bar{y} = 0$$

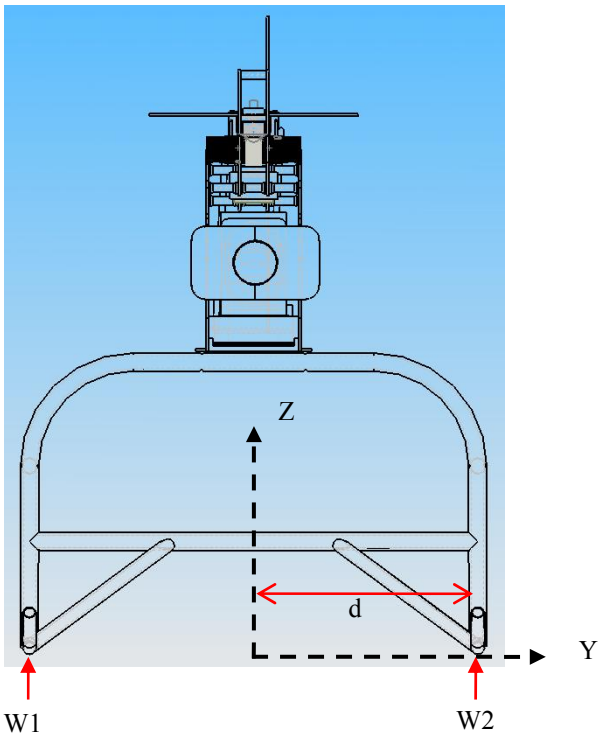

Figure A1: Test procedure for determining the y_{cg}

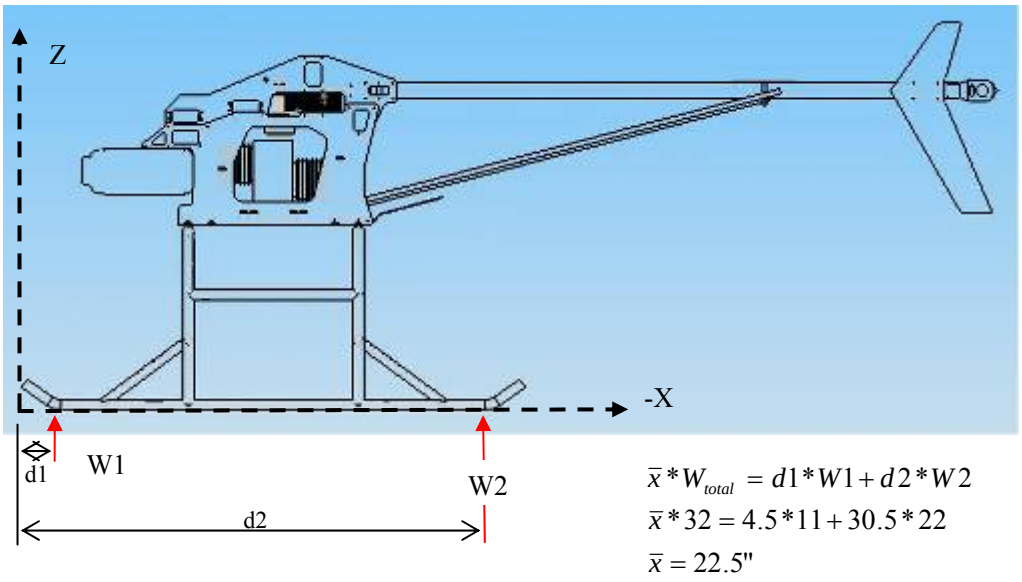

Figure A2: Test procedure for determining the x_{cg}

In determining z_{cg} the helicopter was turned 90 degrees and weighed.

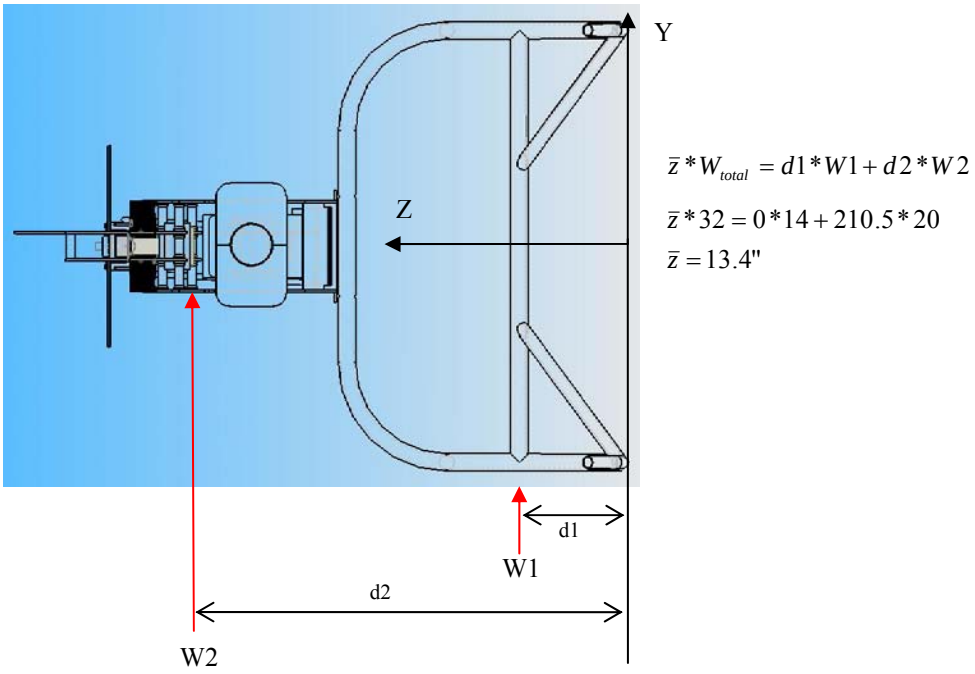

Figure A3: Test procedure for determining the z_{cg}

Moment of Inertia

The moment of inertia tensor was determined experimentally by using a Trifilar and Bifilar Pendulum technique. In this technique oscillatory periods are measured, using a small angle assumption. Figure A4 illustrates the testing process. The Trifilar Pendulum method requires the center of gravity of the platform and object to be aligned. The Bifilar method assumes the axis of rotation passes through the center of mass of the object and is equidistant from the wires.

Conservation of energy for a single degree-of-freedom system yields the equations necessary for determining the moment of inertia. One can say the total change

$$\frac{d}{dt}\left(kinetic\,energy + potential\,energy\right) = 0$$

The kinetic energy term accounts for the mass moment of inertia of the test platform, and any object placed on the platform, and its rotational velocity. The potential energy term accounts for the raising of the platform, and object, in the gravitational field. Utilizing the small angle assumption, the following equations of motion result:

$$J_p\ddot{\theta} + \frac{M_p g R^2}{L}\theta = 0$$

$$\left(J_p + J_o\right)\ddot{\theta} + \frac{\left(M_p + M_o\right)gR^2}{L}\theta = 0$$

where:

- J_p = Mass moment of inertia of platform
- M_p = Mass of platform
- R = Radius of attachment point of wires on platform
- L = Length of wires supporting the platform
- g = Acceleration due to gravity
- J_o = Mass moment of inertia of object

- M_o = Mass of object

These equations exhibit the form of a classic second order linear system. Dividing by the acceleration coefficient brings the equations to the form

$$\ddot{\theta} + \varpi_n^2 \theta$$

where w_n equals $\sqrt{\frac{M_p g R^2}{L J_p}}$. Then rearranging and expressing the natural frequency in term of the period yields

$$J_p = \frac{M_p g R^2 \tau^2}{4 L \pi^2}$$

The same procedure is repeated for the equation representing the platform and object, yielding the object's moment of inertia as

$$J_o = J_p - \frac{\left(M_p + M_o\right) g R^2 \tau^2}{4 \pi^2 L} \theta$$

A uniform wooden disc was used as the platform. The analytical mass moment of inertia is found to equal 0.6312 kg*m^2 while the experimental moment is 0.6118 kg*m^2. Using the same procedure the moments of inertia along the main axis are

I_{xx}	0.32 kg*m^2
I_{yy}	1.43 kg*m^2
I_{zz}	1.21 kg*m^2

Due to symmetry the cross moments I_{xy} and I_{yz} cancel. It is assumed the cross moment Ixz is negligible.

Figure A4a: Trifilar Pendulum Test

Figure A4b: Bifilar Pendulum Test

Appendix B: The 11 Degree of Freedom Model

The need for higher order models stems from the body-roll and blade flap coupling and blade lead-lag motion that exists in rotorcraft at mid to high frequency ranges [8]. The six DOF model well accounts for the low frequency dynamics but breaks down in the mid and high frequency range. In [8] a "hybrid" model is proposed which utilizes the six DOF structure for the low frequency dynamics while incorporating simplified rotor equations which account for the blade flap and lead-lag motion in the mid to high frequency range. The low frequency dynamics are captured by maintaining all six DOF quasi-steady derivatives except for R_p, M_q, R_{lat}, and M_{lon}. The coupling of the fuselage and rotor dynamics is manifest through effective rotor spring derivatives R_{b1s} and M_{a1s}. The lead-lag motion is modeled using a modal approximation [8]. Mathematical relationships for the blade flap and lead-lag motion can be found in [8]. The resulting linearized equations take the form shown in A_{11} and B_{11}. Note that the Euler angles Φ and Θ are included in A_{11} resulting in 13 states.

$$A_{11} = \begin{bmatrix}
X_u & 0 & 0 & 0 & 0 & -g\cos\theta & X_{a1s} & 0 & 0 & 0 & 0 & 0 & 0 \\
0 & Y_v & 0 & 0 & g\cos\theta\cos\phi & 0 & 0 & Y_{b1s} & 0 & 0 & 0 & 0 & 0 \\
R_u & R_v & 0 & 0 & 0 & 0 & 0 & R_{b1s} & R_w & 0 & 0 & 0 & 0 \\
M_u & M_v & 0 & 0 & 0 & 0 & M_{a1s} & 0 & M_w & 0 & 0 & 0 & 0 \\
0 & 0 & 1 & 0 & 0 & 0 & 0 & 0 & 0 & 0 & 0 & 0 & 0 \\
0 & 0 & 0 & 1 & 0 & 0 & 0 & 0 & 0 & 0 & 0 & 0 & 0 \\
0 & 0 & 0 & -\tau_{mr} & 0 & 0 & -1 & A_{b1s} & 0 & 0 & 0 & A_c & 0 \\
0 & 0 & -\tau_{mr} & 0 & 0 & 0 & B_{a1s} & -1 & 0 & 0 & 0 & 0 & B_d \\
0 & 0 & 0 & 0 & 0 & 0 & Z_{a1s} & Z_{b1s} & Z_w & Z_r & 0 & 0 & 0 \\
0 & N_v & N_p & 0 & 0 & 0 & 0 & 0 & N_w & N_r & N_{rfb} & 0 & 0 \\
0 & 0 & 0 & 0 & 0 & 0 & 0 & 0 & 0 & K_r & K_{rfb} & 0 & 0 \\
0 & 0 & 0 & -\tau_{sb} & 0 & 0 & 0 & 0 & 0 & 0 & 0 & -1 & 0 \\
0 & 0 & -\tau_{sb} & 0 & 0 & 0 & 0 & 0 & 0 & 0 & 0 & 0 & -1
\end{bmatrix}$$

$$B_{11} = \begin{bmatrix} 0 & 0 & 0 & 0 \\ 0 & 0 & Y_{tr} & 0 \\ 0 & 0 & 0 & 0 \\ 0 & 0 & 0 & M_{coll} \\ 0 & 0 & 0 & 0 \\ 0 & 0 & 0 & 0 \\ A_{lat} & A_{lon} & 0 & 0 \\ B_{lat} & B_{lon} & 0 & 0 \\ 0 & 0 & 0 & Z_{coll} \\ 0 & 0 & N_{tr} & N_{coll} \\ 0 & 0 & 0 & 0 \\ 0 & C_{lon} & 0 & 0 \\ D_{lat} & 0 & 0 & 0 \end{bmatrix}$$

Appendix C: Response of 6 DOF Model to Step Input

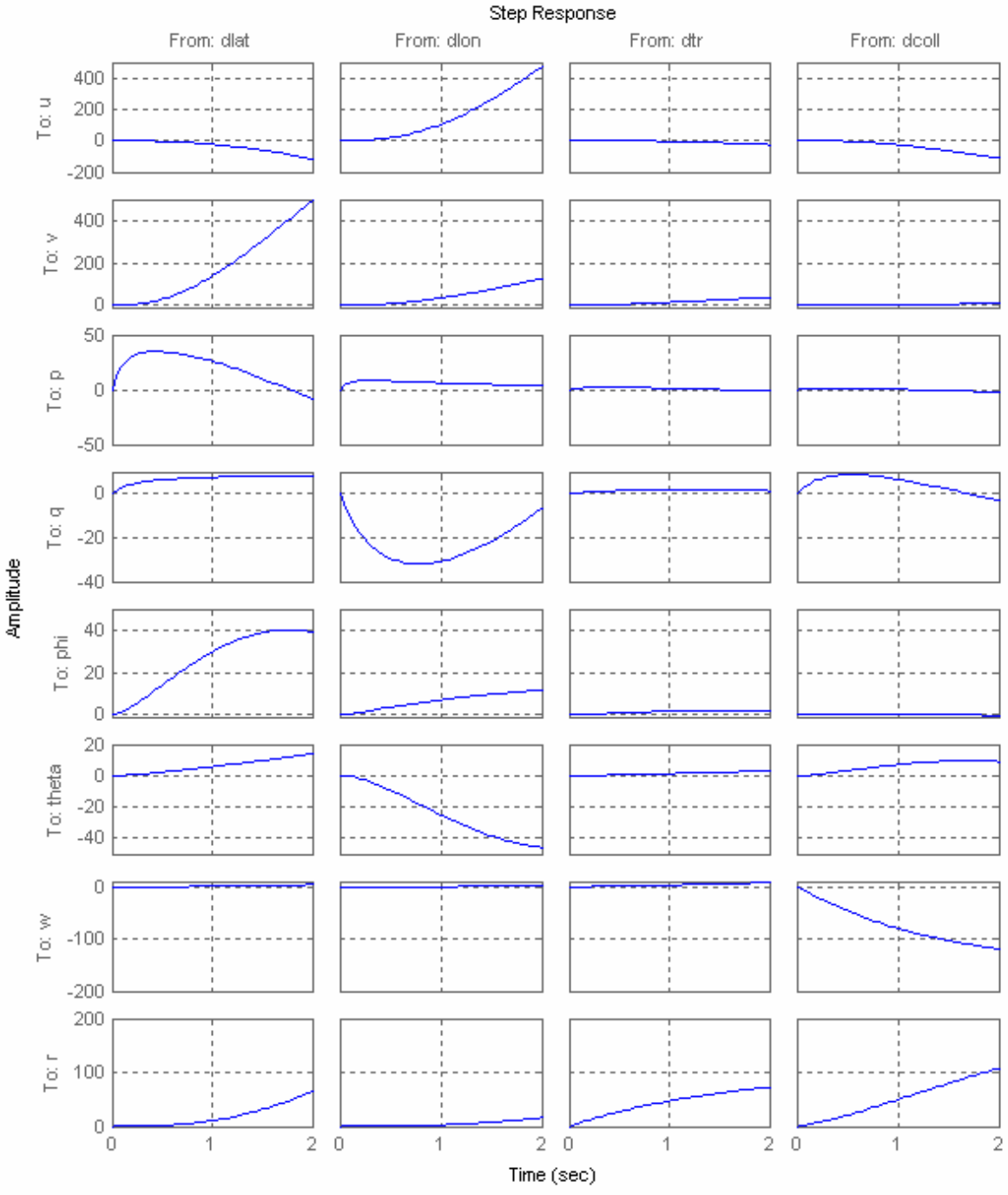

Appendix D: Stability Derivative Values in Hover

Following the methods outlines in [1] the following stability derivative values results for the hover condition.

	u	v	p	q	phi	theta	w	r
X	-0.0129	-0.0018	0.0149	0.1554	0	-9.81	0	0
Y	0.0018	-0.0497	-0.161	0.0149	9.81	0	0	0.0408
R	0.1068	-0.9182	-9.2348	0.8818	0	0	0	0
M	0.277	0.0389	-0.3207	-3.3494	0	0	0.3027	0
phi	0	0	1	0	0	0	0	0
theta	0	0	0	1	0	0	0	0
Z	0	0	0	0	0	0	-0.5876	0.1296
N	0	0.2443	0.0745	0	0	0	-0.7857	-0.6544

	dlat	dlon	dtr	dcoll
X	-1.68	5.64	0	3.42
Y	5.64	1.68	4.78	-0.09
R	267.25	99.78	20.32	-0.75
M	36.28	-121.48	6.43	45.77
phi	0	0	0	0
theta	0	0	0	0
Z	0	0	0	-109.39
N	0	0	63.42	28.40